

BAF complexes drive proliferation and block myogenic differentiation in fusion-positive rhabdomyosarcoma

Dominik Laubscher

University Children's Hospital Zurich

Berkley Gryder

Genetics Branch, NCI, NIH <https://orcid.org/0000-0003-0130-2302>

Benjamin Sunkel

Nationwide Children's Hospital

Thorkell Andresson

Protein Characterization Laboratory of the Cancer Research Technology Program (CRTP)

Sudipto Das

Protein Characterization Laboratory of the Cancer Research Technology Program (CRTP)

Bernd Roschitzki

University of Zurich <https://orcid.org/0000-0001-5756-9773>

Witold Wolski

University of Zurich/ETH Zurich

Xiaoli Wu

Cold Spring Harbor Laboratory

Hsien-chao Chou

National Cancer Institute, National Institutes of Health <https://orcid.org/0000-0002-4870-9663>

Young Song

Genetics Branch, NCI, NIH, Bethesda, MD

Chaoyu Wang

National Cancer Institute

Jun Wei

National Cancer Institute <https://orcid.org/0000-0002-4812-0250>

Meng Wang

Nationwide Children's Hospital

Xinyu Wen

National Cancer Institute

Joana Marques

University Children's Hospital Zurich

Marco Wachtel

University Children's Hospital Zurich

Christopher Vakoc

Cold Spring Harbor Laboratory

Beat Schäfer

University Children's Hospital Zurich <https://orcid.org/0000-0001-5988-2915>

Benjamin Stanton

Nationwide Children's Hospital <https://orcid.org/0000-0002-2613-2955>

Javed Khan (✉ khanjav@mail.nih.gov)

National Cancer Institute <https://orcid.org/0000-0002-5858-0488>

Article

Keywords: Chromatin remodelers, BAF, Rhabdomyosarcoma, Epigenetics, BRG1, myogenesis, MYCN

Posted Date: January 7th, 2021

DOI: <https://doi.org/10.21203/rs.3.rs-131009/v1>

License:  This work is licensed under a Creative Commons Attribution 4.0 International License.

[Read Full License](#)

Version of Record: A version of this preprint was published at Nature Communications on November 26th, 2021. See the published version at <https://doi.org/10.1038/s41467-021-27176-w>.

Abstract

Rhabdomyosarcoma (RMS) is a pediatric malignancy of skeletal muscle lineage. The aggressive alveolar subtype is characterized by t(2;13) or t(1;13) translocations encoding for PAX3- or PAX7-FOXO1 chimeric transcription factors, respectively, and are referred to as fusion positive RMS (FP-RMS). The fusion gene alters the myogenic program and maintains the proliferative state while blocking terminal differentiation. Here we investigated the contributions of chromatin regulatory complexes to FP-RMS tumor maintenance. We define, for the first time, the mSWI/SNF repertoire in FP-RMS. We find that *SMARCA4* (encoding BRG1) is overexpressed in this malignancy compared to skeletal muscle and is essential for cell proliferation. Proteomic studies suggest proximity between PAX3-FOXO1 and BAF complexes, which is further supported by genome-wide binding profiles revealing enhancer colocalization of BAF with core regulatory transcription factors. Further, mSWI/SNF complexes act as sensors of chromatin state and are recruited to sites of *de novo* histone acetylation. Phenotypically, interference with mSWI/SNF complex function induces transcriptional activation of the skeletal muscle differentiation program associated with MYCN enhancer invasion at myogenic target genes which is reproduced by BRG1 targeting compounds. We conclude that inhibition of BRG1 overcomes the differentiation blockade of FP-RMS cells and may provide a therapeutic strategy for this lethal childhood tumor.

Introduction

Cancers in children and young adolescents are fundamentally different from tumors found in adults and have a markedly lower overall mutational burden¹. Pediatric malignancies can be considered as disruptions to normal development² due to epigenetic dysregulation impacting gene expression networks with stabilization of undifferentiated states³. Mechanisms that govern the differentiation of cellular lineages, by mutational independent mechanisms, are often deregulated in childhood tumors⁴. Nucleosome remodeling is essential for gene regulation and is carried out by multi subunit complexes that use energy in form of ATP to change nucleosome position, spacing, and DNA-histone contacts. mSWI/SNF represents a major class of nucleosome modelers and is critical for cancer and development across human tissues⁵⁻⁷.

Rhabdomyosarcoma is the commonest soft tissue tumor in children⁸. Despite the expression of core regulatory myogenic transcription factors, RMS tumor cells are unable to terminally differentiate^{9, 10}. Although historically subdivided into embryonal and alveolar RMS by histological features, biological and clinical differences are better reflected by the presence or absence of oncogenic fusion proteins¹¹. In fusion-positive RMS (FP-RMS), the commonest translocation arises from in-frame fusion events between PAX3 and FOXO1 genes on chromosome 2 and 13, respectively^{12, 13}. While overall survival rates have been greatly improved over the last 30 years, prognosis for FP-RMS has remained dismal due to the aggressive nature of the disease and lack of precision therapies¹¹. This is partly related to a deficit in our understanding of epigenetic drivers and role of ATP-dependent chromatin remodelers in FP-RMS.

Mammalian SWI/SNF (mSWI/SNF) complexes act as major tumor suppressors, carrying genetic alterations in 20% of cancers^{14,15}. Tumor-specific mutations often occur in subunits exclusive to one of the three major mSWI/SNF sub-complexes, canonical BAF (cBAF), Polybromo-associated BAF (PBAF), or non-canonical BAF (ncBAF, alternatively GBAF), suggesting that these specialized complexes have distinct roles in epigenetic mechanisms of tumor suppression in specific cancers¹⁶. Increasing evidence indicates that individual mSWI/SNF complexes can have context-dependent oncogenic functions^{17,18}. In contrast to adult cancers, which bear frequent mutations in mSWI/SNF, pediatric tumors driven by oncogenic fusions often depend on mSWI/SNF activity. Examples include Ewing's Sarcoma that express EWS-FLI1 and MLL-rearranged acute myeloid leukemia (AML) which sustain their transcriptional signatures through mSWI/SNF function¹⁹⁻²¹. PAX3-FOXO1 mediated epigenetic changes maintain the proliferative state in FP-RMS, while at the same time prevent terminal muscle differentiation through direct transcriptional targets of the fusion protein and its capability to induce altered enhancer architecture²²⁻²⁷.

Here we determine which chromatin regulatory complexes contribute to RMS tumor maintenance and demonstrate that BRG1-containing mSWI/SNF complexes are essential in both major RMS subtypes. We further characterize FP-RMS complex composition and their specific genome wide binding patterns. In FP-RMS, interfering with complex function leads to withdrawal from cell cycle and induction of transcriptional and morphological differentiation through invasion of myogenic enhancers by MYCN, causing enhanced transcription. Our study is consistent with previous reports suggesting targeting of ACTL6A (encoding BAF53a) as potential differentiation therapy in RMS²⁸, while our findings reveal that the BRG1 ATPase plays a key role in differentiation block and oncogenesis in FP-RMS.

Results

mSWI/SNF complexes are essential in rhabdomyosarcoma

To investigate the relative importance of different chromatin-regulatory factors for the growth of RMS cells, we performed a CRISPR/Cas9 screen targeting all catalytic and reader domains of chromatin regulatory complexes in fusion negative (FN)-RMS (SMS-CTR and RD) and FP-RMS (RH4 and RH30) cell lines (**Figure 1a**). For both FP-RMS cell lines, we identified the ATPase domain of BRG1 (encoded by *SMARCA4*) as the most essential catalytic domain (**Figure 1b, c**) while the closely related homolog BRM (encoded by *SMARCA2*) did not demonstrate strong dependencies (**Table S1, Figure 1b, c**). In addition, we found moderate dependencies on individual bromodomains of BRG1 and of the PBAF subunit PBRM1 (BD1-6) in RH4 and RH30 cells (**Table S1**). The bromodomain of the ncBAF subunit BRD9 scored as a weak dependency in FP-RMS cells (**Table S1**).

The BRG1 ATPase domain was an essential catalytic domain also in FN-RMS, for both RD and SMS-CTR cells, but ranked comparatively lower than in the FP-RMS models (**Table S1, Figure 1d, e**). FN-RMS cells were each more dependent on other SNF2 family ATPase domains (**Table S1**). Thus, our unbiased CRISPR deletion screens targeting hundreds of regulatory domains and remodeling enzymes, revealed

essential roles for mSWI/SNF complex subunits in RMS and suggest that the BRG1 ATPase domain is the most important catalytic activity in FP-RMS cells, while dependencies on this subunit are less stringent for FN-RMS.

To validate these results, we performed time course competition experiments with guide RNAs targeting SMARCA4 (encoding BRG1), SMARCA2 (encoding BRM), SMARCB1 (encoding BAF47), or PAX3-FOXO1 in RH4 cells expressing active Cas9 (**Figure S1a**). These studies confirmed the sensitivity of FP-RMS cells to PAX3-FOXO1 depletion, and also revealed significant reduction of RH4 cell proliferation upon BRG1, but not BRM depletion, thereby validating our CRISPR/Cas9 domain screens (**Figure 1f,g**). Targeting the non-catalytic BAF47 subunit, a critical mediator of histone interaction and mSWI/SNF nucleosome remodeling activity, also inhibited RH4 proliferation similar to PAX3-FOXO1 targeting (**Figure 1f**). These results suggest that the ncBAF complex, lacking BAF47, is not sufficient to maintain proliferation of FP-RMS cells. Motivated by these observations, we determined the differential expression of these genes compared to normal skeletal muscle from publicly available RNA-seq datasets. We found that *SMARCA4* and *SMARCB1* are overexpressed in RMS, while *SMARCA2* is overexpressed in skeletal muscle compared to RMS tumors (**Figure S1b**). We therefore conclude that in RMS, BRG1 is the major mSWI/SNF ATPase, and that BRM subunit switching may be required for terminal differentiation of skeletal muscle.

Next, we investigated the functional consequences of depleting mSWI/SNF complex subunits and found that there was no induction of apoptosis, as evidenced by lack of PARP or Caspase 7 cleavage at seven days after transduction with sgRNAs, and no effect on PAX3-FOXO1 protein level (**Figure 1h**). However, genetic depletion of BRG1 or BAF47 resulted in a significant increase of cells in G1, accompanied by a significantly reduced percentage of cells progressing through S phase, whereas targeting BRM did not change cell cycle distribution compared to negative control sgRNA (**Figure 1i, Figure S1c**). Taken together, our findings demonstrate that FP-RMS cells depend on intact, functional mSWI/SNF complexes containing the BRG1 ATPase to maintain proliferative states.

PAX3-FOXO1 interacts with mSWI/SNF complexes on chromatin

Given the similar functional dependencies on mSWI/SNF subunits and PAX3-FOXO1 in FP-RMS cells, we sought to understand whether they act through shared spatial proximity in living cells. We used a proximity-labeling approach with BirA fused to PAX3-FOXO1 either at its N- or C-terminus as bait (**Figure S2a,b**)³¹. Proteomic analysis in HEK293T cells after streptavidin immunoprecipitation (IP) identified many mSWI/SNF subunits including BRG1, BRM, BAF47, ACTL6A, SMARCE1, SMARCC1, DPF2, ARID1A, and ARID1B in both approaches (**Figure 2a,b, Table S2a,b**; $\log_2fc > 2.5$, $p < 0.05$). GO-term analysis confirmed top-ranking enrichments of mSWI/SNF complex members over BirA-only background control (**Figure S2c**). Further, enrichment of mSWI/SNF-complex subunits was confirmed by Western Blot together with a positive control interaction partner, PLK1 (**Figure S2d,e**)³². Interestingly, these studies suggested that PAX3-FOXO1 interacts exclusively with the canonical BAF mSWI/SNF subfamily, characterized by incorporation of ARID1 and DPF-family proteins. Although they are expressed in these cells, the absence of PBRM1, ARID2, PHF10, and BRD7 in our BioID dataset suggests the PBAF subfamily

does not share proximity with PAX3-FOXO1. Thus, we show evidence for selective *in vivo* proximity of canonical BAF with PAX3-FOXO1.

To confirm whether BRG1 is proximal to endogenous PAX3-FOXO1, we performed additional co-immunoprecipitation (CoIP) experiments using FP-RMS whole cell extracts. Reciprocal CoIP assays revealed robust interactions between BRG1 and PAX3-FOXO1 in RH4 cells (**Figure 2c**), which was reproducible in RH30 cells (**Figure S2f**, left panel). Interestingly, pre-treatment of whole cell extracts with benzonase, a strong endonuclease, prior to immunoprecipitation reduced the physical interaction observed between BRG1 and PAX3-FOXO1, suggesting their proximity may be mediated in part through DNA/chromatin interactions (**Figure 2c, Figure S2f**)^{33,34}. In addition to BRG1, we also observed DNA/chromatin-dependent interaction of SMARCC1 with PAX3-FOXO1 (**Figure S2f**, right panel). These results confirm interactions between the PAX3-FOXO1 and intact canonical BAF complexes in FP-RMS cells which are possibly mediated through the chromatin interface.

To understand if BRG1-containing complexes mediate PAX3-FOXO1 activity, we next biochemically characterized the repertoire of mSWI/SNF-like complexes assembled in FP-RMS cells. We performed size-exclusion chromatography (SEC) to determine the relative migration and corresponding molecular weight of these complexes from RH4 cells. BRG1- and BAF47-positive fractions (SEC fractions 15-17) eluted above 1 million Daltons (**Figure 2d**). We hypothesized that PBRM1-containing PBAF complexes would elute at higher molecular weight (predicted 4 MDa^{6,35}), but instead we observed similar retention times corresponding to 1-2 MDa for the PBRM1 subunit (**Figure 2d**, SEC fraction 16). Results were replicated in RH30 cells and revealed similar retention times for BRG1, BAF47, and PBRM1, confirming the existence of 1-2 megadalton mSWI/SNF complexes in independent FP-RMS cell models (**Figure 2e**)^{35,36}.

To gain further insight into the assemblies of mSWI/SNF complexes, we performed immunoprecipitation reactions against BRG1 in the 1-2 megadalton SEC fractions, followed by liquid-chromatography mass spectrometry (LCMS). Our proteomic characterization of SEC fractions 16-18 from RH30 and RH4 cells revealed multiple mSWI/SNF-like remodeler subunits in the input and specific IP, but not in the IgG control (**Tables S3,S4**), suggesting that FP-RMS cells express and incorporate subunits that constitute all three of the major mSWI/SNF subfamilies, namely BAF (ARID1A/B, DPF2), PBAF (PBRM1, ARID2, PFH10, BRD7), and ncBAF (BRD9, GLTSCR1) complexes as well as multiple paralogs of the variant subunits within the mSWI/SNF core (SMARCC1/2, SMARCD1/2/3) and ATPase (BCL7A/B/C, SS18/SS18L1) modules (**Figure 2f, Table S4a-d**). Consistent with its minor role in RMS cell proliferation, and low mRNA expression, BRM SEC-IP-LCMS revealed limited incorporation of this alternate ATPase subunit into intact complexes, as only PBRM1, SMARCE1, and SMARCD2 were co-enriched (**Table S4e**). Thus, BRG1-containing complexes in FP-RMS cells represent each of the three major mSWI/SNF subfamilies³⁶.

To address the discrepancy between our observed PBAF molecular weight (1-2 MDa) and previous PBAF molecular weight predictions (~4 MDa), we characterized PBRM1-containing mSWI/SNF complexes following SEC (**Figure 2g**). PBRM1-associated complexes possess the characteristic subunits, including ARID2, PHF10, and BRD7 (**Table S4f,g**), revealing the molecular weight and subunit composition of PBAF

complexes isolated from FP-RMS cells are consistent with the recently defined 1.41 MDa PBAF complex³⁶. Taken together, we find evidence for a remarkably broad range of variant mSWI/SNF assemblies in FP-RMS consistent with BAF, PBAF, ncBAF.

mSWI/SNF complexes mediate myogenic differentiation blockade in FP-RMS

We next investigated whether BRG1-containing complexes would be important for maintenance of anti-differentiation transcriptional networks. We observed an elongated cell morphology 7 days after depletion of BRG1 but not BRM (**Figure 3a**). This morphology was accompanied by cells becoming increasingly myosin heavy chain (MHC) positive, indicative of cellular differentiation (**Figure 3b**).

To confirm this observation, we performed gene set enrichment analysis (GSEA) of RNA-seq data for the same time points after depletion of BRG1, BAF47 and PAX3-FOXO1 compared to negative control (**Figure S3a**). Surprisingly, we found that knockout of both BRG1 and BAF47 led to upregulation of MYC signature genes, which was not seen by PAX3-FOXO1 knockout (**Figure 3c**). We noted that expression of various MYC isoforms was not dramatically increased after either BRG1 or BAF47 knockout (**Figure S3b**), suggesting chromatin-level restructuring. We confirmed upregulation of genes associated with MYOG-dependent super enhancers in both BRG1 and PAX3-FOXO1 knockout conditions, validating activation of the myogenic differentiation program (**Figure 3c**). BAF47 knockout upregulated a smaller subset of myogenic targets (c.f., **Fig. 3d**). To determine whether myogenic differentiation was a consequence of reduced PAX3-FOXO1 activity after mSWI/SNF subunit knockout, we checked global PAX3-FOXO1 target gene expression. Expression of the PAX3-FOXO1 transcription signature was only modestly affected by either BRG1 or BAF47 knockout, while a dramatic reduction of expression was seen by knockout of the fusion protein (**Figure 3c**), arguing for a PAX3-FOXO1 independent regulation of myogenic target genes by mSWI/SNF. To validate induction of terminal differentiation markers, we performed RT-qPCR experiments after knockout of either BRG1, BAF47 or BRM. Expression of myogenic differentiation genes, including myosin heavy/light chains and troponin C2/T3 (*MYL1*, *MYH3/4/8*, *TNNC2*, *TNNT3*), as well as muscle creatine kinase (*CKM*), were significantly induced ($p < 0.05$) upon loss of BRG1 or BAF47, but not BRM (**Figure 3d**). Induction of myosin heavy chains (MHC) upon BRG1 and BAF47 knockout was also validated at the protein level (**Figure S3c**). Integrating our RNA-seq with genomic locations of BRG1 and PAX3-FOXO1 using ChIP-seq, we observed little to no effect of mSWI/SNF knockout on expression of PAX3-FOXO1 bound genes regardless of BRG1 co-occupancy. Similarly, downregulation of these genes by knockout of PAX3-FOXO1 was independent of BRG1 co-localization (**Figure 3e**). Altogether, these results provide evidence that BRG1 containing mSWI/SNF complexes contribute to differentiation blockade in FP-RMS cells without directly affecting PAX3-FOXO1 activity.

Previous findings have shown that BRG1 can serve to refine the expression of core-regulatory transcription factors (CRTFs) in mESCs^{37,38}. To see whether similar events were occurring in FP-RMS cells, we performed spike-in normalized ChIP-seq for BRG1, revealing robust enrichment at *MYOD1*, *MYOG*, and other myogenic loci, which was nearly completely eliminated by BRG1 knockout conditions (**Figure 3f,g, Figure S3d-f**). Supporting a de-repression model, BRG1 loss at the *MYOD1* and *MYOG* loci

coincided with enhanced H3K27ac ChIP-seq signals and a corresponding gain in expression of these myogenic core factors observed by RNA-seq (**Figure 3f,g**). These results suggest that BRG1-containing complexes dial down myogenic gene expression in FP-RMS and their removal promotes transcriptional “amplification” of the core myogenic circuitry.

mSWI/SNF complexes bind to loci associated with core regulatory circuitry

We next investigated the genomic context for the functional dependencies and phenotypic effects observed after BRG1 depletion in FP-RMS cells. Previous studies have revealed that specific mSWI/SNF subcomplexes mediate remodeling of enhancers³⁹⁻⁴¹, and bivalent promoters^{42, 43}. Therefore, we hypothesized that mSWI/SNF binding at FP-RMS core regulatory elements could explain the importance of these complexes.

To test this hypothesis, we began by defining genome-wide binding for PBRM1 and BRG1 in RH4 cells and analytically defined binding overlap with distinct regulatory element classes. Substantial binding of PBRM1 alone was found at active and bivalent promoters exclusively. Sites occupied by both PBRM1 and BRG1 were found predominantly at active promoters, but not bivalent promoters. BRG1 bound sites that lacked PBRM1 localized to active and bivalent promoters but additionally were associated with enhancer elements (**Figure 4a**). This suggested that BAF and ncBAF complexes (that lack PBRM1) have the ability to bind enhancer regions in FP-RMS, locations that are established by the CRTFs PAX3-FOXO1, MYOD1 and MYCN²⁶ (**Figure 4a**).

Prompted by these associations, we further clarified subcomplex specific assemblies by performing additional ChIP-seq experiments for DPF2 and BRD9, allowing us to distinguish BAF (BRG1 and DPF2), PBAF (BRG1 and PBRM1) and ncBAF (BRG1 and BRD9) genomic binding^{36, 44} (**Figure 4b**). Locations occupied by all four proteins are considered to have all 3 complexes (**Figure 4b**) and were the most heavily acetylated among PBAF locations. Locations with canonical BAF that were non-coincident with PBAF were the most accessible (measured by ATAC-seq, **Figure 4b**).

To explore the association with FP-RMS core regulators in more detail, we rigorously defined all combinations of mSWI/SNF complex co-occupancy. We determined that the highest degree of co-binding for PAX3-FOXO1, MYOD1 and MYCN was detected for canonical BAF bound regions (lacking PBAF), which is consistent with our BioID studies. Additionally, ncBAF complexes also showed overlap with CRTFs, but to a lesser extent. Sites containing only PBAF, or other mSWI/SNF subcomplexes together with PBAF, were rarely associated with CRTFs, although they comprise the majority of all mSWI/SNF occupied sites (**Figure 4b,c**). To identify enriched DNA sequence motifs within sites occupied by specific mSWI/SNF complexes, we performed HOMER analysis⁴⁵ (**Figure S4a**). We found that PBAF had substantially different motif preferences compared to BAF and ncBAF complexes. Interestingly, BAF and ncBAF displayed enrichment for CRTF motifs such as PAX3-FOXO1, MYOD1, MYOG as well as MYF5, consistent with its supposed regulatory function within myogenic regulatory circuitries (**Figure S4a**). We noted PAX3-FOXO1 peak strength was significantly higher in BAF co-bound regions, but this only

represented a small fraction (17%) of all PAX3-FOXO1 peaks (**Figure S4b**). Taken together, these results revealed unique binding preferences for individual subtypes of mSWI/SNF complexes and preferential association of BAF with the FP-RMS core regulatory circuitry.

To understand which mSWI/SNF complex subtypes are most important for the induction of myogenic- and MYC-target genes, we examined differential expression levels by RNA-seq after knockout of BRG1, BAF47 or PAX3-FOXO1 and integrated the analysis by evaluating which mSWI/SNF complexes are bound in proximal regulatory elements. We observed that MYC target genes are induced irrespective of mSWI/SNF complex occupancy, in both BRG1 and BAF47 knockout conditions, whereas myogenic genes showed a tendency to be induced more strongly with BAF-only complexes bound at nearby regulatory elements (**Figure S4c**). However, these target genes were more sensitive to PAX3-FOXO1 knockout, independently of mSWI/SNF subclass colocalization (**Figure S4c**). In agreement with previous results, PAX3-FOXO1 target genes associated with SWI/SNF complexes did not show dependency on any of the assemblies (**Figure S4c**). Hence, despite not acting as a major co-factor with PAX3-FOXO1, our results are consistent with BAF complexes contributing to a differentiation blockade through influencing enhancer/promoter-driven myogenic transcriptional networks.

mSWI/SNF binding responds to acetylation levels and limits the myogenic core circuitry

As mSWI/SNF complexes lack intrinsic sequence specificity, their localization patterns are likely specified through recognition of histone modifications via chromatin reader domains or by protein interactions with coactivators. We found that multiple bromodomains are critical for SWI/SNF complex function in FP-RMS (**Figure 1b,c, Table S1**), and hypothesized that these domains may function to target the complexes to sites of H3-acetylation. Having observed overlap of SWI/SNF complexes with H3K27ac and FP-RMS CRTFs (**Figure 4b**), we sought to investigate this phenomenon on a global scale.

We began by characterizing the correlation between BRG1 and the CRTF MYCN, which revealed increased binding of BRG1 at sites with high MYCN occupancy (**Figure 5a**) as exemplified by comparing the *SMARCA4* and *MYOD1* loci (**Figure 5b**). Further dissection revealed positive correlation between MYCN, BRG1, and H3K27ac that was most pronounced at TSS-distal enhancers (**Figure S5a,b**). Notably, global MYCN, BRG1, and H3K27ac sites are most enriched in DNA motifs representing the FP-RMS core circuitry factors MYOD1 and MYOG (**Figure S5c**), supporting the foundational role for these CRTFs in maintenance of the regulatory network^{26,27}.

We therefore tested the hypothesis that mSWI/SNF occupancy could be secondary to CRTF enhancer establishment and responding to local acetylation levels. Spike-in normalized ChIP-seq for BRG1, PBRM1, and H3K27ac following 4-hour treatment with the histone deacetylase (HDAC) inhibitor Entinostat vs. DMSO revealed a global increase in TSS distal H3K27ac signal commensurate with enhanced binding of BRG1 and redistribution of PBRM1 from promoters to these distal regulatory sites (**Figure S5d-h**). Taken together, our results suggest a hierarchy of CRTF establishment of the active regulatory landscape

influencing the acetylation-responsive localization of mSWI/SNF complexes, which may normally function to refine the amplitude of the FP-RMS circuitry (**Figure 5c**).

Having observed the de-repression of *MYOD1* and *MYOG* loci subsequent to BRG1 loss (**Figure 3f,g**), we investigated the involvement of CRTFs in the direct stimulation of the myogenic pathway. Consistent with reported antagonism between MYC-family TFs and mSWI/SNF complexes⁴⁶, we observed enhanced MYCN occupancy at *MYOD1* regulatory elements upon BRG1 knockout (**Figure 5d,e**). Importantly, this “invasion” of the locus by MYCN was reproducible upon ATPase subunit degradation using the recently reported BRG1/BRM-degrading PROTAC, ACBI1⁴⁷ (**Figure 5d,e**). Looking more globally, we found evidence for enhancer invasion occurring across the majority of BRG1 and MYCN co-occupied regions upon both genetic and chemical depletion of BRG1, suggesting a broader alteration of the transcriptional circuitry (**Figure 5f**). Notably, sites co-occupied by MYCN and BRG1 displayed higher MYOD1 and MYOG binding compared to loci only bound by BRG1. (**Figure S5i**). As *MYOD1* and *MYOG* but not *MYCN* are upregulated in response to BRG1 loss (**Figure 3f,g, Figure S3b**), we suggest that redistribution of MYCN to these loci may be secondary to enhanced MYOD1/MYOG occupancy, though we cannot rule out promiscuous yet direct MYCN binding. Connecting the genomic redistribution of CRTFs to the observed myogenic differentiation phenotype, we found that BRG1 knockout had no effect on the expression of genes near its binding sites lacking MYCN, while BRG1-bound genes exhibiting MYCN invasion were upregulated upon BRG1 loss (**Figure 5g**). This was particularly pronounced for genes mapping to the myogenesis pathway, which were additionally bound by MYOD1 and MYOG (**Figure 5g**). Together these data reflect a direct transcriptional “amplification” of the myogenic CRTF circuitry following BRG1 loss.

Interestingly, ChIP-seq for the core SWI/SNF subunit SMARCC1, revealed possible retention of residual chromatin remodeling complexes at sites of CRTF invasion in the absence of BRG1 (**Figure S5j**). We found that upon genetic depletion of BRG1, these sites showed a general increase in H3K27ac levels, while PROTAC treatment, degrading both BRG1 and BRM, did not result in H3K27ac accumulation (**Figure S5j**). These findings suggest a potential role for BRM subunit switching into the mSWI/SNF complex, as compensatory for BRG1 loss, causing relief of the differentiation blockade.

Rapid BRG1 ablation in FP-RMS phenocopies genetic inactivation of BAF function

To expand our studies beyond experimental genetic knockdown approaches, we wanted to examine pharmacological small molecule inhibitors of mSWI/SNF ATPases to validate our phenotypic findings in additional FP-RMS cell lines (RH4, RH5, RHJT). Therefore, we used either an allosteric ATPase inhibitor (ATPi)⁴⁸, or the proteolysis targeting chimera (PROTAC) compound ACBI1⁴⁷ (insert schemes **Figure 6**).

We observed that both compounds (ATPi at low micromolar and PROTAC nanomolar levels) led to elongated cell morphology (**Figure 6a, d**) indicative of ongoing myogenic differentiation. To confirm that the expression of muscle differentiation genes is upregulated upon ATPi treatment, we performed RT-qPCR analysis. Several markers such as myosin heavy (*MYH4/8*) and light chains (*MYL1*) as well as muscle creatine kinase (*CKM*) and myocyte enhancer factor 2C (*MEF2C*) were induced reproducibly in all

FP-RMS cell lines (**Figure 6b**). We observed increased expression of the same myogenic marker genes as well as *MYOD1*, *MYOG* and Troponin T3 (*TNNT3*) with PROTAC treatment (**Figure 6e**). To confirm that altered cell morphologies are indeed accompanied by elevated expression of myosin heavy chains (MHC), we performed immunofluorescence staining after drug treatment. We found that, compared to control treatment, FP-RMS cells became increasingly MHC positive, predominantly in cells with elongated shapes (**Figure 6c,f**). Although the effects of PROTAC treatment were less pronounced in RHJT, we found similar tendencies compared to the other FP-RMS cell lines. (**Figure 6d-f**).

We confirmed the efficacy of protein degradation by ACBI1 PROTAC in both FP-and also FN-RMS cells (**Figure S6a,b**). However, despite similar reduction in both BRG1 and BRM protein levels, the phenotypic effects were different in FN-RMS cells from FP-RMS cells. FN-RMS cells were less sensitive to compound treatment (**Figure S6d**) and did not show any morphological signs of myogenic differentiation (**Figure S6f**), which was confirmed by RT-qPCR (**Figure S6g**). We obtained the same results also with ATPase inhibitor treatment of FN-RMS cells (**Figure S6c,e,g**). In addition, myogenic differentiation marker genes were also not induced upon BRG1 knockdown in RD FN-RMS cells (**Figure S6h**). These findings are consistent with the BRG1 ATPase having a specific role to block differentiation in FP-RMS cells. To conclude, we were able to show that pharmacological BRG1/BRM disrupting compound treatments phenocopied the effects observed by genetic interference studies, suggesting that the effects we observe may be direct consequences of BAF inactivation.

To summarize our overall findings, we have uncovered indications that sustained expression of *SMARCA4* (encoding BRG1), which is markedly lower in normal muscle tissue, contributes to keeping FP-RMS cells in an undifferentiated state by dampening myogenic core regulatory transcription factor activity (**Figure 6g**). This blockade can be overcome by genetic or PROTAC (ACBI1) induced BRG1 depletion as well as inhibition of its ATPase activity (ATPi) (**Figure 6g**).

Discussion

Alveolar rhabdomyosarcoma is driven by the presence of the oncogenic transcription factor PAX3-FOXO1. The widely-held model suggests that RMS originates from the skeletal muscle lineage, based on the expression of myogenic regulatory factors (MRFs)^{9, 49}. The chimeric fusion oncogene is an initiating event^{50, 51} and maintains its transcriptional circuitry through cooperation with CRTFs such as MYCN, MYOD1, MYOG and SOX8. Recent evidence furthermore suggests that HDACs are integral to the core regulatory circuitry (CRC) in FP-RMS^{26, 27, 52}. Consequently, FP-RMS displays an altered epigenetic landscape to sustain proliferative capacity and block myogenic differentiation. Although epigenetic repression of myogenic promoters^{22, 24, 53}, and maintenance of CRC through enhancer architecture^{25, 52} have been shown to contribute to this phenomenon, precise mechanistic links to ATP-dependent chromatin remodeling complexes have remained elusive. Our work provides insights into the contribution of BRG1 containing BAF complexes for stabilization of the myogenic anti-differentiation phenotype in FP-RMS. This has implications for the basic understanding of mSWI/SNF in human tumors, as well as for precision therapies.

Notably, the SNF2-like ATPases most highly mutated in adult tumors⁵⁴ closely mirror the dependencies for the wild-type ATPases in FP-RMS as reported here. Non-mutated mSWI/SNF complexes were shown to drive oncogenic gene expression programs in pediatric tumors characterized by other fusion transcription factors¹⁹⁻²¹. Similarly, gain-of-function mSWI/SNF alterations in synovial sarcoma maintain anti-differentiation transcription signatures⁵⁵⁻⁵⁷. In this context, FP-RMS is associated with a similar pattern of low mutational burden¹, with expression of wt-mSWI/SNF complexes. The fact that we found BRG1 to be prominently overexpressed in FP-RMS compared to skeletal muscle is in agreement with its oncogenic functions in other cancers¹⁷. The relatively moderate dependency on individual bromodomains observed in our screening could be explained by partial compensatory effects. This is concordant with findings showing that ATPase domains surpass bromodomains as drug targets in mSWI/SNF mutant cancers⁵⁸.

We describe here the most comprehensive characterization of mSWI/SNF assemblies in FP-RMS cells and show evidence for all three major complex classes (cBAF, pBAF, ncBAF). Notably, different compositions of mSWI/SNF complexes have been associated in specific stages of myogenesis⁵⁹, reminiscent of miRNA-mediated subunit exchange during neuronal differentiation⁶⁰. We demonstrate that mSWI/SNF complex assemblies in FP-RMS cells have the characteristics of undifferentiated muscle, exemplified by expression and complex incorporation of all three SMARCD1/2/3 isoforms, while subunit exchange in favor of SMARCD3 drives normal skeletal and cardiac muscle programs⁶¹⁻⁶³. Stage-specific roles of the two ATPases during myogenesis have also been reported⁶⁴ and is concordant with BRG1 domination in less differentiated cells.

We have shown that interference with BRG1-containing mSWI/SNF complex function in FP-RMS leads to proliferation defects and characteristic morphological and transcriptional changes indicating relief from differentiation blockade. This stands in agreement with previously reported findings showing downregulation of ACTL6A induces differentiation in RMS cells²⁸.

We describe the genomic binding patterns of mSWI/SNF complexes in FP-RMS and find that BAF complexes associate with CRTFs (PAX3-FOXO1, MYCN and MYOD1) because of their binding to enhancer regions. We demonstrate that mSWI/SNF complexes are recruited to sites of *de novo* histone acetylation, as may be the case during CRTF driven super-enhancer establishment²⁶. We therefore propose that deposition of H3K27ac at myogenic enhancers recruits BAF complexes. This concept may lend additional mechanistic insight into the sensitivity of FP-RMS cells to HDAC inhibitors²⁷, as these compounds may disrupt the “acetylation sensor” function of the essential SWI/SNF complexes. Whether genomic localization of BAF complexes is altered by PAX3-FOXO1 through phase separation processes, similar to retargeting by EWS-FLI1 in Ewing’s sarcoma^{19,65}, remains to be determined. However, we exclude a global co-regulatory function of SWI/SNF complexes and PAX3-FOXO1 based on our RNA-Seq, proteomics, and ChIP-seq findings. Nevertheless, myogenic differentiation genes are also induced by knockout of the fusion protein, suggesting regulation through a different route.

BRG1 depletion at regulatory elements of genes important for myogenic differentiation (e.g. MYOG, MYOD1) coincided with increased expression and H3K27ac levels. This observation is consistent with a tonic repressive function of BRG1 complexes, as has been described previously in human embryonic stem cells⁶⁶. Together with our observations of H3-acetylation sensing, mutually reinforcing influence between mSWI/SNF and chromatin acetylation is possible. Despite being a rather counterintuitive finding, functional antagonism between MYC/MYCN and mSWI/SNF components is consistent with recent reports describing BAF47-associated reduction of MYC binding and ARID1A-dependent suppression of MYCN induced tumorigenesis^{46, 67}. Indeed, we saw increased MYCN binding after BRG1 removal at many sites, which is correlated with a boost in transcriptional activity at myogenic target genes. The fact that MRF motifs are enriched at BRG1 as well as MYCN bound loci suggests that these factors might act together to regulate myogenic gene expression. These findings implicate that BRG1 complexes act to tonically repress MYCN binding in concert with restricting the expression of myogenic transcription factors such as MYOD1 and MYOG to lock tumor cells in a proliferative state.

Although FN-RMS cells were moderately sensitive to BRG1 depletion in our CRISPR screens, we saw induction of myogenic differentiation only in PAX3-FOXO1 positive RMS. This indicates that different rhabdomyosarcoma subtypes have evolved different strategies to sustain their de-differentiated phenotype. The difference could be attributed to distinct requirements for remodeling downstream of RAS activation compared to PAX3-FOXO1 mediated functions. It is possible that FP-RMS differentiation is blocked at the *MYOD1* and other myogenic loci by BAF related tonic repression of MYCN binding at its super enhancers, in contrast to the known FN-RMS block via ERK signaling at the TSS of *MYOG*⁶⁸.

It is of note that BRM depletion did not lead to any proliferation or differentiation phenotypes in our experiments. It has been shown that the two mSWI/SNF ATPases can have unique functions and might discordantly regulate gene sets, target classes, or genome architecture⁶⁹. Therefore, BRM might substitute for BRG1 loss but functionally antagonize or regulate unique loci to induce cell cycle arrest and terminal differentiation⁶⁴. However, this model requires further investigation as the same differentiation phenotype is induced by simultaneous inhibition of BRG1/BRM with PROTAC or inhibitors. Nevertheless, there is residual SMARCC1 present at loci after BRG1 knockout or dual BRG1/BRM removal. Thus, while our studies provide evidence consistent with subunit switching with BRM-containing mSWI/SNF assemblies driving differentiation after BRG1 loss, further work is necessary to define these residual complexes.

Vulnerability towards inhibition of the regulatory ATPases of mSWI/SNF complexes has been described in other cancer types and the development of small molecules directed against BRG1 and BRM has been promoted in recent years^{17, 18, 70}. Given our observation that SMARCA4-containing BAF complexes seem to be most important to repress myogenic differentiation in FP-RMS, the avenue to selectively inhibit ARID1A containing assemblies⁷¹ deserves attention in future studies.

In conclusion our we propose a model where sustained expression of SMARCA4 (encoding BRG1) keeps FP-RMS cells in an undifferentiated state by dampening myogenic core regulatory transcription factor

activity. Therefore, our results suggest BRG1 as an essential target whose inhibition may overcome the differentiation blockade in FP-RMS cells, providing new therapeutic opportunities for this highly malignant childhood cancer.

Methods

Cell Lines

The cell lines RH4, RHJT, RH36 (Peter Houghton, Greehey Children's Cancer Research Institute, San Antonio, TX), RH5 (Susan Ragsdale, St. Jude Children's Hospital, Memphis, TN), RH30, RD as well as HEK293T cells (ATCC, LGC Promochem) and SMS-CTR were cultured in DMEM (Sigma-Aldrich), supplemented with 100 U/mL penicillin/streptomycin, 2 mmol/L l-glutamine, and 10% FBS (Life Technologies) in 5% CO₂ at 37°C. Cell lines were controlled for mycoplasma contamination using the LookOut Mycoplasma PCR Detection Kit (Sigma-Aldrich) and were tested negative. All RMS cell lines were authenticated by short tandem repeat analysis (STR) profiling in 2014/2015 and positively matched⁷².

Lentivirus production and transduction

HEK293T cells were seeded in T-25 flasks and transfected the next day with 2,8µg of both the lentiviral envelope (capsid) and packaging plasmid, pCMV-VSV-G and psPAX2, respectively (Addgene) together with 7.4µg of the lentiCRISPR plasmid of interest (**Table S5A**) using the calcium phosphate technique. Medium was changed 24h after transfection and lentiviral supernatant was collected 3 days after transfection, filtered through 0.45µm filter syringes and concentrated using Amicon Ultra tubes (100kDa, Merck). Lentivirus aliquots were either stored at -80°C or directly used to transduce target cells. Target cells were plated in 24-well plates and transduced the day after with virus in culture medium supplemented with 8µg/ml of Polybrene (TR-1003-G, Merck).

CRISPR knockout

Cas9 expressing RH4 cells were generated by transduction of wildtype cells with lentiviral vector coding Cas9 and mNeonGreen (Addgene) followed by sorting. Activity of Cas9 in these cells was tested using Cas9 activity reporter with BFP (Addgene). The lentiviral vectors coding individual sgRNAs (**Table S5A**) were generated by cloning single guide sequences using the In-Fusion cloning system (Clontech, 638909) into the sg_shuttle_RFP657 vector (Addgene). After transduction of Cas9 expressing cells, efficiency of sgRNA delivery was assessed by flow cytometry. Knockout of individual target genes was validated by western blot analysis at indicated timepoints.

CRISPR competition assay

Cas9 expressing RH4 cells (GFP positive) were plated in 24-well format and transduced the next day with sgRNA carrying lentiviruses (with RFP reporter). 2 days after transduction, cells were mixed with same amount of untransduced cells. Part of the resulting mixture was directly used for baseline flow cytometry measurements, while the rest was kept in culture. For flow cytometry analysis, cells were fixed with 0.5% Paraformaldehyde/1xPBS and washed twice in 1xPBS. After resuspension of cell pellets in 1xPBS, samples were analyzed using the BD LSR Fortessa instrument. GFP and RFP signals were acquired to assess percentages of transduced cell populations. Wildtype, untransduced as well as Cas9 expressing RH4 cells were used to set gates and/or compensation respectively. Data were analyzed with FlowJoV10 software. Dead cells and doublets were excluded by manual gating. Measurements were repeated after 7 and 12 days post transduction to follow the development of populations carrying either control or gene targeting sgRNAs (**Table S5A**). Finally, percentages of RFP positive cell populations were normalized to baseline measurements obtained at day 2.

qRT-PCR

Total RNA was extracted using the Qiagen RNeasy Plus Mini Kit (Qiagen) and reverse-transcribed using oligo (dT) primers and Omniscript reverse transcriptase (Qiagen). qRT-PCR was performed for gene specific TaqMan assays indicated in **Table S5C** using TaqMan gene expression master mix (all Life Technologies). Data were analyzed with the SDS 2.4 software. Cycle threshold (CT) values were compared to GAPDH. Relative expression levels were calculated using the $\Delta\Delta CT$ method based on 3 technical replicates. Outliers found in technical replicates ($SD > 0.5$) were removed from the analysis. Mean and upper and lower limit values were calculated for the indicated amounts of biological replicates.

RNA-seq and GSEA

Biological triplicate samples of Cas9 expressing RH4 transduced with indicated sgRNAs were collected 7 days after transduction for RNA isolation. Total RNAs were extracted by RNeasy Plus Mini Kit (Qiagen). Paired-end mRNA libraries were prepared using Truseq Stranded Total RNA Library Prep Kit (Illumina) and sequenced on a Novaseq system as 2x150 base reads by Atlas Biolab GmbH (Berlin, Germany).

RNA-seq reads were mapped to the human genome build hg19 by STAR (<https://github.com/alexdobin/STAR>) and quantified as Transcription Per Million (TPM) or Fragments Per Kilobase Million (FPKM) using RSEM (<https://deweylab.github.io/RSEM/>). Gene set enrichment was assessed using GSEA software (<https://www.gsea-msigdb.org/gsea/>) and visualized in R (<https://github.com/GryderArt/VisualizeRNAseq>).

BioID experiments

Plasmids for expression of N- and C-terminal BirA-Flag fusion constructs⁷³ were a kind gift of Philip Knobel (Laboratory for Applied Radiobiology, University Zurich). BirA-Flag/PAX3-FOXO1 fusion constructs were generated by amplification of a prevalidated PAX3-FOXO1 cDNA, using primers including restriction sites for *Ascl* (forward) and *NotI* (reverse), and cloned into N- or C-terminal BirA-Flag backbone vectors. Transient transfection of BirA-Flag/PAX3-FOXO1 fusion constructs or BirA-Flag alone into HEK293T cells was conducted using PEI reagent. Expression as well as subcellular localization of proteins were confirmed by western blot or Immunofluorescence respectively. For Streptavidin Immunoprecipitations, 7.5 Mio. HEK293T cells were plated in a 15cm plate. The next day, cells were transfected with 12.6µg of plasmid DNA in presence or absence of 50µM Biotin. Biotin stock solution (20mM) was obtained by dissolving 100mg of powder (IBA, 2-1016-002) in 2.04ml of NH₄OH 28-30% (Sigma Aldrich, ref# 221228), 18ml of 1M HCl was added to neutralize the solution (pH~7.5) and stored at 4°C. 24h after transfection, cells were harvested by scraping in 1xPBS. After washing once with 1xPBS, cell pellets were resuspended in 1.5ml Lysis buffer (**Table S5F**) supplemented with 250U of Benzonase (Novagen, 70664). Lysates were incubated for 1h at 4°C under rotation. After brief sonication to disrupt visible aggregates, centrifugation was performed at 16000g for 30min at 4°C. Cleared input samples were incubated together with 75ul Dynabeads MyOne Streptavidin T1 (Thermo Fisher, 65601) per plate for 2h at 4°C under rotation. For subsequent western blot analysis immunoprecipitates were washed three times with Lysis buffer and eluted from the beads in 1X NuPAGE LDS sample buffer (Thermo Fisher, LuBioScience) at 70°C. For downstream proteomic experiments, beads were washed once in lysis buffer followed by two washing steps with 50mM ammonium bicarbonate. Beads were resuspended in 150µl of 50mM ammonium bicarbonate, snap-frozen and stored at -80°C. For on-bead digestion, 8M urea/100mM Tris-HCl pH8.2 was added to a final concentration of 2M urea. Reduction and Alkylation were carried out using 2mM TCEP and 10mM Chloracetamide for 1h at 30°C under agitation in the dark. The solutions were diluted with Tris-HCl pH8.2 in a 1/1 ratio and digestion was performed with 1µg trypsin per sample overnight at 30°C under agitation in the dark. The next day, supernatant was taken from the beads and pooled with two washing steps with 100ul 10%ACN/Tris-HCl (final concentration of 3%ACN) and acidified to 0.5% TFA. Sample cleanup was performed using Sep-Pack C18 columns and completely dried using speed vac centrifugation. Samples were dissolved in LC-MS solution (3% ACN; 0.1% FA) for further analysis.

Mass Spectrometry: Dissolved samples were injected by an Easy-nLC 1000 system (Thermo Scientific) and separated on an EasySpray-column (75 µm x 500 mm) packed with C18 material (PepMap, C18, 100 Å, 2 µm, Thermo Scientific). The column was equilibrated with 100% solvent A (0.1% formic acid (FA) in water). Peptides were eluted using the following gradient of solvent B (0.1% FA in ACN): 5-25% B in, 60 min; 25-35% B in 10 min; 35-99% B in 5 min at a flow rate of 0.3 µl/min. All precursor signals were recorded in the Orbitrap using quadrupole transmission in the mass range of 300-1500 m/z. Spectra were recorded with a resolution of 120 000 at 200 m/z, a target value of 5E5 and the maximum cycle time was set to 3 seconds. Data dependent MS/MS were recorded in the linear ion trap using quadrupole isolation

with a window of 1.6 Da and HCD fragmentation with 30% fragmentation energy. The ion trap was operated in rapid scan mode with a target value of 8E3 and a maximum injection time of 80 ms. Precursor signals were selected for fragmentation with a charge state from +2 to +7 and a signal intensity of at least 5E3. A dynamic exclusion list was used for 25 seconds. After data collection peak lists were generated using FCC⁷⁴ and Proteome Discoverer 2.1 (Thermo Scientific).

Proteomic Data Analysis: The acquired raw MS data were processed by MaxQuant (version 1.6.2.3), followed by protein identification using the integrated Andromeda search engine⁷⁵. Spectra were searched against a Uniprot human reference proteome (taxonomy 9606, canonical version from 2016-12-09), concatenated to its reversed decoyed fasta database and common protein contaminants. Carbamidomethylation of cysteine was set as fixed modification, while methionine oxidation and N-terminal protein acetylation were set as variable. Enzyme specificity was set to trypsin/P allowing a minimal peptide length of 7 amino acids and a maximum of two missed-cleavages. MaxQuant Orbitrap default search settings were used. The maximum false discovery rate (FDR) was set to 0.01 for peptides and 0.05 for proteins. Label free quantification was enabled and a 2 minutes window for match between runs was applied. In the MaxQuant experimental design template, each file is kept separate in the experimental design to obtain individual quantitative values. Protein fold changes were computed based on Intensity values reported in the proteinGroups.txt file. A set of functions implemented in the R package SRMServe⁷⁶ was used to filter for proteins with 2 or more peptides allowing for a maximum of 4 missing values, and to normalize the data with a modified robust z-score transformation and to compute p-values and fold changes using the limma package⁷⁷. If all measurements of a protein are missing in one of the conditions, a pseudo fold change was computed, replacing the missing group average by the mean of 10% smallest protein intensities in that condition.

Immunoblotting

Total cell extracts were obtained with RIPA buffer (**Table S5F**). Protein concentration was measured with Pierce BCA protein Assay Kit (Thermo Fisher Scientific). Proteins were separated using 4%–12% Bis-Tris SDS-PAGE gels (Thermo Fisher Scientific, LuBioScience) and transferred to nitrocellulose membranes (GE Healthcare). After blocking with 5% milk powder in TBS/0.1% Tween, membranes were incubated with primary antibodies overnight at 4°C. After washing in TBS/0.1% Tween, membranes were incubated with HRP-linked IgG antibodies for 1h at room temperature. Proteins were detected by chemiluminescence using ECL detection reagent or SuperSignal West Femto Maximum Sensitivity Substrate (both Thermo Fisher Scientific) after washing in TBS/0.1% Tween. All antibodies used for Western Blot are indicated in **Table S5B**.

Co-Immunoprecipitation

Cells were lysed in 2ml Lysis buffer (**Table S5F**) per 15-cm dish. Lysates were incubated for 2h at 4°C, with antibody directed against the protein of interest coupled to Dynabeads Protein G (Thermo Fisher Scientific, 10003D) or empty beads as negative control. Antibodies used for CoIPs are indicated in **Table S5B**. Benzonase (Novagen, 70664) was added to the lysate during this incubation when indicated. After washing 4 times with lysis buffer, proteins were eluted with 1x NuPAGE LDS sample buffer (Thermo Fisher Scientific) at 70°C and analyzed by Western blotting using EasyBlot reagents (Genetex, GTX425858 and GTX221666-01).

Immunofluorescence

Cas9 expressing RH4 cells were transduced with indicated sgRNA as described above. Cells were plated onto chamber slides and immunofluorescence was performed after 7 days post transduction. For experiments with BirA constructs, immunofluorescence was carried out the day after transfection as described above. After washing with 1xPBS, cells were fixed with 4% Formalin followed by washing and quenching with 0.1M Glycine/PBS. Cells were washed 3 more times with 1xPBS and permeabilized with 0.1% Triton X-100/PBS and blocked using 4% horse serum in 0.1% Triton X-100/PBS. Incubation with primary antibody dissolved in 4% horse serum in 0.1% Triton X-100/PBS was done overnight in a humid chamber. The next day, secondary antibodies were added in 4% horse serum/PBS for 1h. Antibodies used for Immunofluorescence are indicated in **Table S5B**. After washing 3 times with 1xPBS, slides were embedded and counterstained with Vectashield/DAPI solution (Vector Laboratories, H-1200) and sealed with nail polish.

Cell cycle analysis

Cas9 expressing RH4 cells were transduced with indicated sgRNAs as described above. Cells were harvested by trypsinization, washed in 1xPBS, fixed in 70% ice-cold Ethanol and incubated at -20°C for at least 2 hours. Before flow cytometry, cells were washed by PBS and resuspended in 500µl PI solution (**Table S5F**). Data were processed by FlowJoV10 software using Dean-Jett-Fox model to assign cell cycle phases.

ChIP experiments

ChIP reactions to determine SWI/SNF subcomplex genomic binding under basal and Entinostat treated conditions were performed according to established protocols^{42, 78, 79}. For detailed compositions of buffers used refer to Table S5F.

ChIP assays for SWI/SNF interference studies were performed using the iDeal ChIP-seq kit for Transcription Factors (Diagenode) according to the manufacturer's instructions. Briefly, Cas9 expressing RH4 cells were transduced with indicated sgRNAs. Alternatively, cells were treated with 250nM ACBI1 or cis conformation negative control compound (**Table S5E**) respectively. After expansion of cells at 7 days post transduction/treatment, cells were fixed using a dual step protocol with ChIP Cross-link Gold (Diagenode, C01019027) for 30min followed by 1% formaldehyde for 15 min, harvested and sonicated with the Bioruptor Pico sonication device (Diagenode) for 13 cycles (30sec ON, 30sec OFF). Sonicated lysates were then quantified and 25µg (35µg for MYCN ChIP) of chromatin were spiked-in with *Drosophila* Chromatin (Active Motif) and incubated overnight at 4°C with 4µg (7µg for MYCN ChIP) of antibody and an antibody against the *Drosophila* specific histone variant H2Av (Active Motif) (**Table S5B**). Amounts of spike-in components were calculated according to manufacturers instructions. As these agents are introduced at identical amounts and concentrations during the ChIP reactions, technical variation associated with downstream steps is accounted for.

After DNA purification, library preparation was performed as previously described⁷⁹. DNA libraries were prepared using TruSeq ChIP Library Prep Kit (Illumina, IP-202–1012). DNA was size selected with SPRI select reagent kit (to obtain a 250–300 bp long fragments). Then, libraries were multiplexed and sequenced using NextSeq500 High Output Kit v2 (Illumina, FC-404–2005) on an Illumina NextSeq500 machine. All libraries were quantified using a Qubit fluorimeter to measure concentration and sequenced on NextSeq platform with single-end reads.

For ChIP-qPCR experiments, DNA was purified and qPCR reactions were set up using PowerUp SYBR Green Master Mix (ThermoFisher) with loci specific primers (**Table S5D**) according to the manufacturer's instructions. Relative amounts of immunoprecipitated DNA compared to INPUT DNA was calculated using the formula; %recovery = $2^{[(Ct(input)-\log_2(X)-Ct(sample))]} \times 100\%$ whereby X accounts for input dilution. For comparison of same antibody ChIPs between different conditions, Ct values obtained with *Drosophila* specific Pgbs primer set (Active Motif) were used to correct for technical variation ($Ct(sample)_{corr} = Ct(sample) - (Ct(sample)_{Pgbs} - Ct(control)_{Pgbs})$). For quantification normalized to control conditions, dCt values = $(Ct(input) - \log_2(X) - Ct(sample))$ were used to calculate relative ddCt values = $dCt(control) - dCt(sample)$ and fold changes were generated by computing $2^{(-ddCt)}$.

Analysis of ChIP-seq datasets

For ChIP studies, analysis was performed as previously reported²⁷. ChIP-seq data was mapped to hg19 using BWA⁸⁰. For ChIP-Rx, we additionally mapped spike in reads to dm3 using BWA⁸⁰, and normalized human reads to million-mapped *Drosophila* reads (RRPM, reference normalize reads per million)⁸¹. Peaks were called using MACS2.0 (<https://github.com/taoliu/MACS>), with stringency thresholds of $p = 0.0000001$ and filtered to remove ENCODE blacklisted regions (<https://sites.google.com/site/anshulkundaje/projects/blacklists>). Peak intersections we identified using

bedtools intersect⁸², and the resulting heatmaps and metagene plots were plotted using deeptools (<https://deeptools.readthedocs.io/en/develop/>). Genome tracks were visualized in IGV⁸³ (<https://www.broadinstitute.org/igv/igvtools>). We performed HOMER for motif analysis⁴⁵ to define enriched TF binding sites within datasets.

WST-1 assays

Cells were cultured in a 384-well format and the day after, treatment with titrated concentrations of indicated compounds (**Table S5E**) was performed using the HP D300e digital dispenser platform. Their viability was measured by WST-1 assay 72 hours after transfection. Cells were incubated with the Cell Proliferation Reagent WST-1 (Roche) for at least 20 min and absorbance was measured in a plate reader at 640nm and 440nm.

Size exclusion chromatography (SEC)/IP-MS experiments

Isolation of nuclear extracts: Nuclear extracts from RH4, RH30, RH4-PAX3-FOXO1-FLAG t(2;13) rhabdomyosarcoma cell models were prepared as previously reported^{35, 38, 42, 57, 84}. Briefly, 10-20 million cells were washed in PBS, and subsequently trypsinized for dissociation. The trypsin was quenched with DMEM with 10% FBS, pelleted (centrifugation, 4⁰C, 180g), and washed again in PBS. After decanting, cells were resuspended in 1 mL Buffer A (**Table S5F**) and diluted with Buffer A to a final volume of 10 mL. Cells were incubated on ice for 7 minutes and pelleted by centrifugation at 1000g. After decanting, pellets were resuspended in 600 mL Buffer C (**Table S5F**). To this suspension was added 66.6 mL ammonium sulfate (3M solution, Sigma, Cat# A4418) and rotated at 4⁰C for 30 minutes. The suspensions were pelleted with ultracentrifugation (100,000 rpm) in 1 mL thick-wall polycarbonate tubes (Beckman Coulter Cat# 343778) at 4⁰C for 11 minutes. After pelleting chromatin, the supernatant was transferred to new thick-wall polycarbonate tubes, into which 200 mg ammonium sulfate was suspended. The suspensions were incubated on ice for 20 minutes, ultracentrifuged at 100,000 rpm for 11 minutes, and nuclear fraction was used for further size exclusion chromatography experiments (SEC; Protein Characterization Laboratory, Cancer Research Technology Program, Frederick National Laboratory).

Size exclusion chromatography: One hundred ug of nuclear extract were size fractionated on Acquity I Class UPLC (Waters), using BioSep SEC 300 (7.8x300 mm) size exclusion column (Phenomenex), equilibrated with 150 mM NaPO₄ pH 7.2. The proteins were eluted from the column using 150 mM NaPO₄ pH 7.2 at 350 ul/minute. Fraction size was estimated by running the Bio Rad gel filtration standard (MW 1,350 to 670,000).

Immunoprecipitation: After size-exclusion chromatography (SEC) for fractionation of nuclear extracts, immunoprecipitation was performed on fractions that stained positive for BAF or PBAF by western

blotting. Briefly, 500 mL SEC fractions were diluted 1:1 (v/v) in SEC-IP buffer (**Table S5F**) and incubated with 3 mg antibody (**Table S5B**) and rotated gently at 4⁰C for approximately 16 hours. To the mixtures, Protein A Dynabeads (ThermoFisher Cat# 10002D) was added and incubated for an additional 4 hours at 4⁰C with rotation. Immunoprecipitation reactions were washed successively with ice cold SEC-IP buffer, and then twice with LCMS buffer (**Table S5F**). Beads were resuspended in 30 mL LCMS buffer and used subsequently for LCMS experiments.

On Bead Trypsin Digestion: The beads were resuspended in 25 mM NH₄HCO₃, pH 8.4 and heated at 95⁰C for 5 min to denature the proteins. The samples were digested overnight with 2 mg of trypsin at 37⁰C. The supernatant containing the tryptic digest was collected after centrifugation of the beads, the beads were washed twice with 25 mM NH₄HCO₃, pH 8.4 and the supernatant and the wash combined for maximum recovery. The peptides were desalted using C18 columns (Thermo Scientific, CA) and lyophilized.

Nanoflow LC and Mass spectrometry: The dried peptides were reconstituted in 0.1%TFA and subjected to nanoflow liquid chromatography (Thermo Easy nLC 1000, Thermo Scientific) coupled to high resolution tandem MS (Q Exactive, HF, Thermo Scientific). MS scans were performed in the Orbitrap analyser at a resolution of 60,000 with an ion accumulation target set at 3e⁶ over a mass range of 380-1580 m/z, followed by MS/MS analysis at a resolution of 15,000 with an ion accumulation target set at 2e⁵. MS2 precursor isolation width was set at 1.4 m/z, normalized collision energy at 27, and charge state one and unassigned charge states were excluded.

Proteomics Data Processing: The raw data was searched against the full human uniprot protein database using the SEQUEST algorithm in the Proteome Discoverer 2.2 software (Thermo Scientific, CA). The precursor ion tolerance was set at 10 ppm and the fragment ions tolerance was set at 0.02 Da along with methionine oxidation included as dynamic modification. Only fully tryptic peptides with up to two mis-cleavages and FDR of 1% using the percolator validator algorithms were accepted.

CRISPR domain screening experiments

For our experiments to define essential domains in rhabdomyosarcoma, we performed pooled CRISPR screens as previously reported^{27, 85, 86}. We targeted the domains of chromatin regulatory complexes in our studies, with specific guide RNAs in pooled experiments (**Table S1**). Our screens included the human SWI/SNF-like ATPase domains (SMARCA4 ATPase, CHD4 ATPase, SRCAP ATPase, INO80 ATPase, TTF2 ATPase, EP400 ATPase, CHD8 ATPase, CHD2 ATPase, ATRX ATPase, CHD6 ATPase, RAD54L ATPase, HLTf ATPase, CHD1 ATPase, SMARCA2 ATPase, CHD7 ATPase, CHD1L ATPase, CHD5 ATPase, ERCC6 ATPase, CHD3 ATPase, SHPRH ATPase, SMARCAD1 ATPase, RAD54L2 ATPase, CHD9 ATPase, HELLS ATPase, SMARCAL1 ATPase). Additionally, our CRISPR targets included bromodomains incorporated into human chromatin regulatory complexes (BRD4, PBRM, TAF1, CREBBP, KAT2A, TRIM28, SMARCA4, BRD8, BPTF, BRD9, EP300, ZMYND8, BAZ1B, BAZ2A, BRD3, ASH1L, TRIM33, SP140, PhIP,

BRDT, SP140L, ATA2B, BRD1, CECR2, BRPF1, SP100, SMARCA2, ATAD2, TRIM24, BRWD1, BRPF3, BRD2, BRWD3, BAZ1A, KAT2B, TRIM66, BAZ2B, KMT2A, ZMYND11). In these experiments, negative and positive control guide RNAs (sgRNAs) were included as internal standards and cloned into lentiviral expression vectors for comparison to the sgRNAs targeting domains in chromatin regulatory complexes. After expression of sgRNAs in RH4, RH30, CTR, or RD cells expression Cas9, harvesting for genomic DNA was carried out 3-days after lentiviral transduction and again at approximately 12 days after transduction. Relative comparison of enrichments for specific targeting sgRNAs and control sgRNAs was carried out by PCR amplification of guide RNAs from genomic DNA, and indexing with custom barcodes as previously reported²⁷, and library amplification for sequencing on the MiSeq platform (Illumina). Relative read counts corresponding to individual sgRNA sequences were normalized to total read depth per sample, and fold enrichments (dependencies) for individual chromatin regulatory domains were determined.

Public datasets analyzed in this study

For this study we used the ENCODE Consortium (<https://sites.google.com/site/anshulkundaje/projects/blacklists>) dataset, as well as two ChIP-seq datasets recently reported^{26, 27} (GSE116344, GSE83725; GEO Omnibus). Additionally, we used gene expression datasets (phs000720; GEO Omnibus and phs001928; dbGAP).

Data availability

The data sets of RNA-seq and ChIP-seq generated in this study have been deposited in the Gene Expression Omnibus database with accession number GSE162052 (Release date set to Dec. 31, 2021).

The mass spectrometry proteomics data of our BioID experiments supporting the findings in Figure 2A,B have been deposited to the ProteomeXchange Consortium via the PRIDE⁸⁷ partner repository with the dataset identifier PXD022187. Reviewer account details:

The mass spectrometry proteomics data of SEC-IP-MS experiments supporting the findings in Figure 2F-H have been made publicly available and were deposited to the ProteomeXchange Consortium via the MassIVE partner repository with the dataset identifier MSV000086494.

Code availability

We have made our code available on github (<https://github.com/GryderArt>), as open-source software for genomics data analysis (including integration of algorithms such as BCHNV, ROSE2, EDEN, COLTRON).

These pipelines are build using Bowtie2⁸⁸, MACS2⁸⁹, DESeq2⁹⁰, and for visualization R-Studio was used (<https://www.rstudio.com/products/RStudio/>).

Reagents or Resources used in this study

Detailed information about Materials and Reagent resources can be found in Supplementary Table S5

Acknowledgements

We want to thank Philip Knobel for providing us with the plasmids and resources as well as protocols related to BioID experiments. We further thank Gloria Pedot for her help to establish RH4 and RD Cas9 NG cell lines by cell sorting. We thank Yun Huan for sharing negative control sgRNA plasmids.

The work was supported by grants from the Swiss National Science Foundation (3100-156923 and 3100-175558) and the Childhood Cancer Research Foundation Switzerland to BS.

BEG, TA, SD, H-CC, YKS, CW, JSW, XW, and JK funded by the Intramural Research Program (IRP) of the National Institutes of Health, National Cancer Institute, Center for Cancer Research. B.Z.S. gratefully acknowledges the St. Baldrick's Foundation (Berry Strong fund), The Andrew McDonough B+ Foundation (Childhood Cancer Research Grant), and Nationwide Children's Hospital for support to understand etiology of childhood cancers.

References

1. Gröbner, S.N. *et al.* The landscape of genomic alterations across childhood cancers. *Nature* **555**, 321–327 (2018).
2. Maris, J.M. & Denny, C.T. Focus on embryonal malignancies. *Cancer Cell* **2**, 447–450 (2002).
3. Panditharatna, E. & Filbin, M.G. The growing role of epigenetics in childhood cancers. *Curr Opin Pediatr* **32**, 67–75 (2020).
4. Ma, X. *et al.* Pan-cancer genome and transcriptome analyses of 1,699 paediatric leukaemias and solid tumours. *Nature* **555**, 371–376 (2018).
5. Hargreaves, D.C. & Crabtree, G.R. ATP-dependent chromatin remodeling: genetics, genomics and mechanisms. *Cell Res* **21**, 396–420 (2011).
6. Lessard, J. *et al.* An essential switch in subunit composition of a chromatin remodeling complex during neural development. *Neuron* **55**, 201–215 (2007).
7. Alfert, A., Moreno, N. & Kerl, K. The BAF complex in development and disease. *Epigenetics Chromatin* **12**, 19 (2019).
8. Ognjanovic, S., Linabery, A.M., Charbonneau, B. & Ross, J.A. Trends in childhood rhabdomyosarcoma incidence and survival in the United States, 1975–2005. *Cancer* **115**, 4218–4226 (2009).

9. Sebire, N.J. & Malone, M. Myogenin and MyoD1 expression in paediatric rhabdomyosarcomas. *J Clin Pathol* **56**, 412–416 (2003).
10. Keller, C. & Guttridge, D.C. Mechanisms of impaired differentiation in rhabdomyosarcoma. *FEBS J* **280**, 4323–4334 (2013).
11. Skapek, S.X. *et al.* Rhabdomyosarcoma. *Nat Rev Dis Primers* **5**, 1 (2019).
12. Marshall, A.D. & Grosveld, G.C. Alveolar rhabdomyosarcoma - The molecular drivers of PAX3/7-FOXO1-induced tumorigenesis. *Skelet Muscle* **2**, 25 (2012).
13. Parham, D.M. & Barr, F.G. Classification of rhabdomyosarcoma and its molecular basis. *Adv Anat Pathol* **20**, 387–397 (2013).
14. Kadoch, C. & Crabtree, G.R. Mammalian SWI/SNF chromatin remodeling complexes and cancer: Mechanistic insights gained from human genomics. *Sci Adv* **1**, e1500447 (2015).
15. Shain, A.H. & Pollack, J.R. The spectrum of SWI/SNF mutations, ubiquitous in human cancers. *PLoS One* **8**, e55119 (2013).
16. Centore, R.C., Sandoval, G.J., Soares, L.M.M., Kadoch, C. & Chan, H.M. Mammalian SWI/SNF Chromatin Remodeling Complexes: Emerging Mechanisms and Therapeutic Strategies. *Trends Genet* (2020).
17. Wu, Q. *et al.* The BRG1 ATPase of human SWI/SNF chromatin remodeling enzymes as a driver of cancer. *Epigenomics* **9**, 919–931 (2017).
18. Hohmann, A.F. & Vakoc, C.R. A rationale to target the SWI/SNF complex for cancer therapy. *Trends Genet* **30**, 356–363 (2014).
19. Boulay, G. *et al.* Cancer-Specific Retargeting of BAF Complexes by a Prion-like Domain. *Cell* **171**, 163–178 e119 (2017).
20. Buscarlet, M. *et al.* Essential role of BRG, the ATPase subunit of BAF chromatin remodeling complexes, in leukemia maintenance. *Blood* **123**, 1720–1728 (2014).
21. Shi, J. *et al.* Role of SWI/SNF in acute leukemia maintenance and enhancer-mediated Myc regulation. *Genes Dev* **27**, 2648–2662 (2013).
22. Walters, Z.S. *et al.* JARID2 is a direct target of the PAX3-FOXO1 fusion protein and inhibits myogenic differentiation of rhabdomyosarcoma cells. *Oncogene* **33**, 1148–1157 (2014).
23. Skrzypek, K. *et al.* SNAIL is a key regulator of alveolar rhabdomyosarcoma tumor growth and differentiation through repression of MYF5 and MYOD function. *Cell Death Dis* **9**, 643 (2018).
24. Lee, M.H., Jothi, M., Gudkov, A.V. & Mal, A.K. Histone methyltransferase KMT1A restrains entry of alveolar rhabdomyosarcoma cells into a myogenic differentiated state. *Cancer Res* **71**, 3921–3931 (2011).
25. Gryder, B.E. *et al.* Miswired Enhancer Logic Drives a Cancer of the Muscle Lineage. *iScience* **23**, 101103 (2020).
26. Gryder, B.E. *et al.* PAX3-FOXO1 Establishes Myogenic Super Enhancers and Confers BET Bromodomain Vulnerability. *Cancer Discov* **7**, 884–899 (2017).

27. Gryder, B.E. *et al.* Histone hyperacetylation disrupts core gene regulatory architecture in rhabdomyosarcoma. *Nat Genet* **51**, 1714–1722 (2019).
28. Taulli, R. *et al.* Failure to downregulate the BAF53a subunit of the SWI/SNF chromatin remodeling complex contributes to the differentiation block in rhabdomyosarcoma. *Oncogene* **33**, 2354–2362 (2014).
29. He, S. *et al.* Structure of nucleosome-bound human BAF complex. *Science* **367**, 875–881 (2020).
30. Wagner, F.R. *et al.* Structure of SWI/SNF chromatin remodeller RSC bound to a nucleosome. *Nature* **579**, 448–451 (2020).
31. Varnaité, R. & MacNeill, S.A. Meet the neighbors: Mapping local protein interactomes by proximity-dependent labeling with BioID. *Proteomics* **16**, 2503–2518 (2016).
32. Thalhammer, V. *et al.* PLK1 phosphorylates PAX3-FOXO1, the inhibition of which triggers regression of alveolar Rhabdomyosarcoma. *Cancer Res* **75**, 98–110 (2015).
33. Stanton, B.Z., Chory, E.J. & Crabtree, G.R. Chemically induced proximity in biology and medicine. *Science* **359** (2018).
34. Douglass, E.F., Jr., Miller, C.J., Sparer, G., Shapiro, H. & Spiegel, D.A. A comprehensive mathematical model for three-body binding equilibria. *J Am Chem Soc* **135**, 6092–6099 (2013).
35. Kadoch, C. *et al.* Proteomic and bioinformatic analysis of mammalian SWI/SNF complexes identifies extensive roles in human malignancy. *Nat Genet* **45**, 592–601 (2013).
36. Mashtalir, N. *et al.* Modular Organization and Assembly of SWI/SNF Family Chromatin Remodeling Complexes. *Cell* **175**, 1272–1288 e1220 (2018).
37. Ho, L. *et al.* An embryonic stem cell chromatin remodeling complex, esBAF, is an essential component of the core pluripotency transcriptional network. *Proc Natl Acad Sci U S A* **106**, 5187–5191 (2009).
38. Ho, L. *et al.* An embryonic stem cell chromatin remodeling complex, esBAF, is essential for embryonic stem cell self-renewal and pluripotency. *Proc Natl Acad Sci U S A* **106**, 5181–5186 (2009).
39. Hodges, H.C. *et al.* Dominant-negative SMARCA4 mutants alter the accessibility landscape of tissue-unrestricted enhancers. *Nat Struct Mol Biol* **25**, 61–72 (2018).
40. Mathur, R. *et al.* ARID1A loss impairs enhancer-mediated gene regulation and drives colon cancer in mice. *Nat Genet* **49**, 296–302 (2017).
41. Wang, X. *et al.* SMARCB1-mediated SWI/SNF complex function is essential for enhancer regulation. *Nat Genet* **49**, 289–295 (2017).
42. Stanton, B.Z. *et al.* Smarca4 ATPase mutations disrupt direct eviction of PRC1 from chromatin. *Nat Genet* **49**, 282–288 (2017).
43. Kadoch, C. *et al.* Dynamics of BAF-Polycomb complex opposition on heterochromatin in normal and oncogenic states. *Nat Genet* **49**, 213–222 (2017).
44. Michel, B.C. *et al.* A non-canonical SWI/SNF complex is a synthetic lethal target in cancers driven by BAF complex perturbation. *Nat Cell Biol* **20**, 1410–1420 (2018).

45. Heinz, S. *et al.* Simple combinations of lineage-determining transcription factors prime cis-regulatory elements required for macrophage and B cell identities. *Mol Cell* **38**, 576–589 (2010).
46. Weissmiller, A.M. *et al.* Inhibition of MYC by the SMARCB1 tumor suppressor. *Nat Commun* **10**, 2014 (2019).
47. Farnaby, W. *et al.* BAF complex vulnerabilities in cancer demonstrated via structure-based PROTAC design. *Nat Chem Biol* **15**, 672–680 (2019).
48. Papillon, J.P.N. *et al.* Discovery of Orally Active Inhibitors of Brahma Homolog (BRM)/SMARCA2 ATPase Activity for the Treatment of Brahma Related Gene 1 (BRG1)/SMARCA4-Mutant Cancers. *J Med Chem* **61**, 10155–10172 (2018).
49. Tonin, P.N., Scrable, H., Shimada, H. & Cavenee, W.K. Muscle-specific gene expression in rhabdomyosarcomas and stages of human fetal skeletal muscle development. *Cancer Res* **51**, 5100–5106 (1991).
50. Barr, F.G. *et al.* Rearrangement of the PAX3 paired box gene in the paediatric solid tumour alveolar rhabdomyosarcoma. *Nat Genet* **3**, 113–117 (1993).
51. Davis, R.J., D'Cruz, C.M., Lovell, M.A., Biegel, J.A. & Barr, F.G. Fusion of PAX7 to FKHR by the variant t(1;13)(p36;q14) translocation in alveolar rhabdomyosarcoma. *Cancer Res* **54**, 2869–2872 (1994).
52. Gryder, B.E. *et al.* Chemical genomics reveals histone deacetylases are required for core regulatory transcription. *Nat Commun* **10**, 3004 (2019).
53. Calhabeu, F., Hayashi, S., Morgan, J.E., Relaix, F. & Zammit, P.S. Alveolar rhabdomyosarcoma-associated proteins PAX3/FOXO1A and PAX7/FOXO1A suppress the transcriptional activity of MyoD-target genes in muscle stem cells. *Oncogene* **32**, 651–662 (2013).
54. Hodges, C., Kirkland, J.G. & Crabtree, G.R. The Many Roles of BAF (mSWI/SNF) and PBAF Complexes in Cancer. *Cold Spring Harb Perspect Med* **6** (2016).
55. McBride, M.J. *et al.* The SS18-SSX Fusion Oncoprotein Hijacks BAF Complex Targeting and Function to Drive Synovial Sarcoma. *Cancer Cell* **33**, 1128–1141 e1127 (2018).
56. Banito, A. *et al.* The SS18-SSX Oncoprotein Hijacks KDM2B-PRC1.1 to Drive Synovial Sarcoma. *Cancer Cell* **33**, 527–541 e528 (2018).
57. Kadoch, C. & Crabtree, G.R. Reversible disruption of mSWI/SNF (BAF) complexes by the SS18-SSX oncogenic fusion in synovial sarcoma. *Cell* **153**, 71–85 (2013).
58. Vangamudi, B. *et al.* The SMARCA2/4 ATPase Domain Surpasses the Bromodomain as a Drug Target in SWI/SNF-Mutant Cancers: Insights from cDNA Rescue and PFI-3 Inhibitor Studies. *Cancer Res* **75**, 3865–3878 (2015).
59. Albin, S. & Puri, P.L. SWI/SNF complexes, chromatin remodeling and skeletal myogenesis: it's time to exchange! *Exp Cell Res* **316**, 3073–3080 (2010).
60. Yoo, A.S., Staahl, B.T., Chen, L. & Crabtree, G.R. MicroRNA-mediated switching of chromatin-remodelling complexes in neural development. *Nature* **460**, 642–646 (2009).

61. Goljanek-Whysall, K. *et al.* Regulation of multiple target genes by miR-1 and miR-206 is pivotal for C2C12 myoblast differentiation. *J Cell Sci* **125**, 3590–3600 (2012).
62. Puri, P.L. & Mercola, M. BAF60 A, B, and Cs of muscle determination and renewal. *Genes Dev* **26**, 2673–2683 (2012).
63. Goljanek-Whysall, K. *et al.* myomiR-dependent switching of BAF60 variant incorporation into Brg1 chromatin remodeling complexes during embryo myogenesis. *Development* **141**, 3378–3387 (2014).
64. Albini, S. *et al.* Brahma is required for cell cycle arrest and late muscle gene expression during skeletal myogenesis. *EMBO Rep* **16**, 1037–1050 (2015).
65. Lindén, M. *et al.* FET family fusion oncoproteins target the SWI/SNF chromatin remodeling complex. *EMBO Rep* **20** (2019).
66. Zhang, X. *et al.* Transcriptional repression by the BRG1-SWI/SNF complex affects the pluripotency of human embryonic stem cells. *Stem Cell Reports* **3**, 460–474 (2014).
67. Shi, H. *et al.* ARID1A loss in neuroblastoma promotes the adrenergic-to-mesenchymal transition by regulating enhancer-mediated gene expression. *Sci Adv* **6**, eaaz3440 (2020).
68. Yohe, M.E. *et al.* MEK inhibition induces MYOG and remodels super-enhancers in RAS-driven rhabdomyosarcoma. *Sci Transl Med* **10** (2018).
69. Raab, J.R., Runge, J.S., Spear, C.C. & Magnuson, T. Co-regulation of transcription by BRG1 and BRM, two mutually exclusive SWI/SNF ATPase subunits. *Epigenetics Chromatin* **10**, 62 (2017).
70. St Pierre, R. & Kadoch, C. Mammalian SWI/SNF complexes in cancer: emerging therapeutic opportunities. *Curr Opin Genet Dev* **42**, 56–67 (2017).
71. Chory, E.J. *et al.* Chemical Inhibitors of a Selective SWI/SNF Function Synergize with ATR Inhibition in Cancer Cell Killing. *ACS Chem Biol* **15**, 1685–1696 (2020).
72. Hinson, A.R. *et al.* Human rhabdomyosarcoma cell lines for rhabdomyosarcoma research: utility and pitfalls. *Front Oncol* **3**, 183 (2013).
73. Silva, J. *et al.* EXD2 governs germ stem cell homeostasis and lifespan by promoting mitoribosome integrity and translation. *Nat Cell Biol* **20**, 162–174 (2018).
74. Barkow-Oesterreicher, S., Türker, C. & Panse, C. FCC - An automated rule-based processing tool for life science data. *Source Code Biol Med* **8**, 3 (2013).
75. Cox, J. & Mann, M. MaxQuant enables high peptide identification rates, individualized p.p.b.-range mass accuracies and proteome-wide protein quantification. *Nat Biotechnol* **26**, 1367–1372 (2008).
76. W. Wolski, J.G., C. Panse (<http://github.com/protViz/SRMService>; 2018).
77. Ritchie, M.E. *et al.* limma powers differential expression analyses for RNA-sequencing and microarray studies. *Nucleic Acids Res* **43**, e47 (2015).
78. Barski, A. *et al.* High-resolution profiling of histone methylations in the human genome. *Cell* **129**, 823–837 (2007).
79. Kidder, B.L. & Zhao, K. Efficient library preparation for next-generation sequencing analysis of genome-wide epigenetic and transcriptional landscapes in embryonic stem cells. *Methods Mol Biol*

- 1150, 3–20 (2014).
80. Langmead, B., Trapnell, C., Pop, M. & Salzberg, S.L. Ultrafast and memory-efficient alignment of short DNA sequences to the human genome. *Genome Biol* **10**, R25 (2009).
 81. Orlando, D.A. *et al.* Quantitative ChIP-Seq normalization reveals global modulation of the epigenome. *Cell Rep* **9**, 1163–1170 (2014).
 82. Quinlan, A.R. & Hall, I.M. BEDTools: a flexible suite of utilities for comparing genomic features. *Bioinformatics* **26**, 841–842 (2010).
 83. Robinson, J.T. *et al.* Integrative genomics viewer. *Nat Biotechnol* **29**, 24–26 (2011).
 84. Wu, J.I. *et al.* Regulation of dendritic development by neuron-specific chromatin remodeling complexes. *Neuron* **56**, 94–108 (2007).
 85. Tarumoto, Y. *et al.* LKB1, Salt-Inducible Kinases, and MEF2C Are Linked Dependencies in Acute Myeloid Leukemia. *Mol Cell* **69**, 1017–1027 e1016 (2018).
 86. Shi, J. *et al.* Discovery of cancer drug targets by CRISPR-Cas9 screening of protein domains. *Nat Biotechnol* **33**, 661–667 (2015).
 87. Perez-Riverol, Y. *et al.* The PRIDE database and related tools and resources in 2019: improving support for quantification data. *Nucleic Acids Res* **47**, D442–D450 (2019).
 88. Langmead, B. & Salzberg, S.L. Fast gapped-read alignment with Bowtie 2. *Nat Methods* **9**, 357–359 (2012).
 89. Zhang, Y. *et al.* Model-based analysis of ChIP-Seq (MACS). *Genome Biol* **9**, R137 (2008).
 90. Love, M.I., Huber, W. & Anders, S. Moderated estimation of fold change and dispersion for RNA-seq data with DESeq2. *Genome Biol* **15**, 550 (2014).
 91. Zhou, Y. *et al.* Metascape provides a biologist-oriented resource for the analysis of systems-level datasets. *Nat Commun* **10**, 1523 (2019).

Additional Information

*These authors contributed equally to this work as shared co-first authors

†Corresponding co-last authors:

Benjamin Z. Stanton, Ph.D. Benjamin.Stanton@nationwidechildrens.org

Beat Schäfer, Ph.D. Beat.Schaefer@kispi.uzh.ch

Javed Khan, M.D. khanjav@mail.nih.gov

All authors declare no conflicts of interest.

Author contribution: DL, BEG, BDS, XSW, SD, YKS and BZS carried out the experiments. DL performed all single gene CRISPR knockout experiments including competition assays, western blots, cell cycle analysis, RNA collection and qPCR analysis, CHIP reactions and qPCR analysis as well as Immunofluorescence. DL conducted BioID experiments, CoIPs and all experiments related to compound treatments. BDS and BZS performed SEC-IP-MS experiments and CHIP reactions for characterization of mSWI/SNF binding. YKS and CW performed sequencing experiments; BEG, HCC, and BDS designed bioinformatic pipelines and performed analysis of sequencing data. JK assisted in performing comparative expression profiling. DL, BEG, BDS, MeW, BWS, and BZS contributed to the analysis and interpretation of the data. TR, BR and WW assisted in acquiring and analysis of proteomic data. XSW and CRV conducted the CRISPR domain screenings. JSW, XW, TA and SD submitted data to the public databases and contributed to manuscript editing. DL, BEG BDS, JSW, BWS, BZS, and JK made substantial contribution to the writing and editing of the manuscript. JGM, MaW, BWS, BS, BZS and JK made substantial contributions to the conception, design and intellectual content. DL, BEG and BZS wrote the paper and prepared the final figures.

Figures

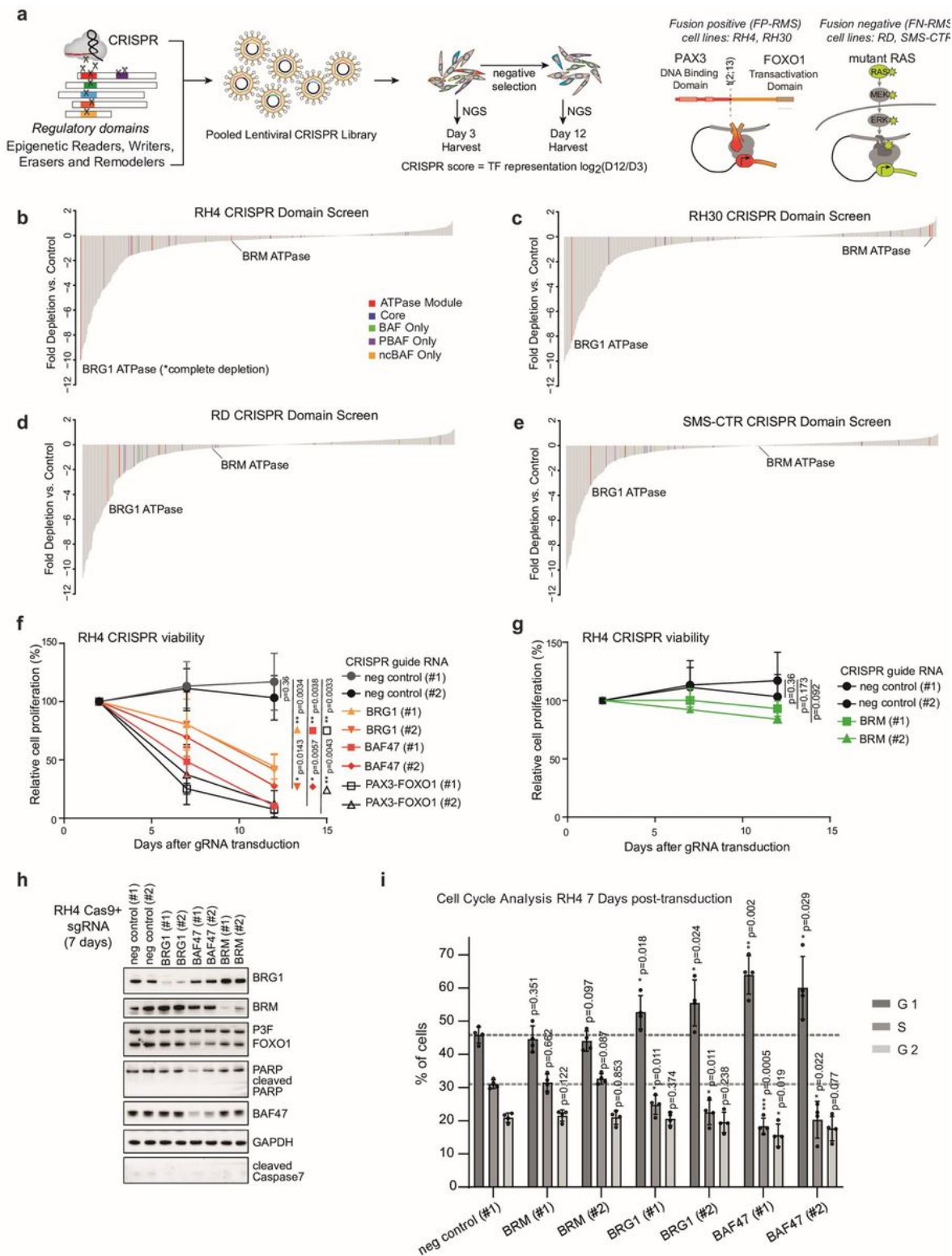


Figure 1

mSWI/SNF complexes are essential in fusion-positive rhabdomyosarcoma. (a) Schematic representation of CRISPR library screening against chromatin regulatory domains performed in FP-RMS and FN-RMS cell lines. Main oncogenic driving aberrations include the PAX3-FOXO1 fusion transcription factor for FP-RMS and RAS mutations for FN-RMS. (b & c) The ranked domain dependencies of RH4 and RH30, patient derived FP-RMS cell lines with t(2;13) from CRISPR screens. (d & e) The ranked domain dependencies in

RD and SMS-CTR, fusion-negative (FN) RMS patient derived cell lines, from CRISPR screens. Fold target depletion versus control values are indicated. Members of mSWI/SNF complexes are highlighted in color code according to subcomplex/assembly specificity. (f & g) Relative proliferative (%) capacities of Cas9 expressing RH4 cell populations transduced with indicated sgRNAs determined by flow cytometry. Data points represent the evolution of transduced cell populations compared to untransduced cells in co-culture. Values are normalized to the starting point of the experiment (day 2 after transduction). Mean and standard deviation values are indicated for 4 independent biological replicates. Statistical significance (rounded to last decimal) is given for the endpoint of the experiment (day 12 after transduction) by paired t-tests (* $p \leq 0.05$, ** $p \leq 0.01$). (h) Western blot analysis of whole cell lysates 7 days after transduction of Cas9 expressing RH4 cells with indicated sgRNAs. BRG1, BRM and BAF47 protein levels are displayed for appreciation of sgRNA efficiencies. GAPDH protein was used as a loading control. (i) Cell cycle effects measured 7 days after transduction of Cas9 expressing RH4 cells with indicated sgRNAs by means of PI staining. Mean and SD values are given for at least 4 different biological replicates. Statistical significance (rounded to last decimal) is given compared to negative control by paired t-tests (* $p \leq 0.05$, ** $p \leq 0.01$, *** $p \leq 0.001$).

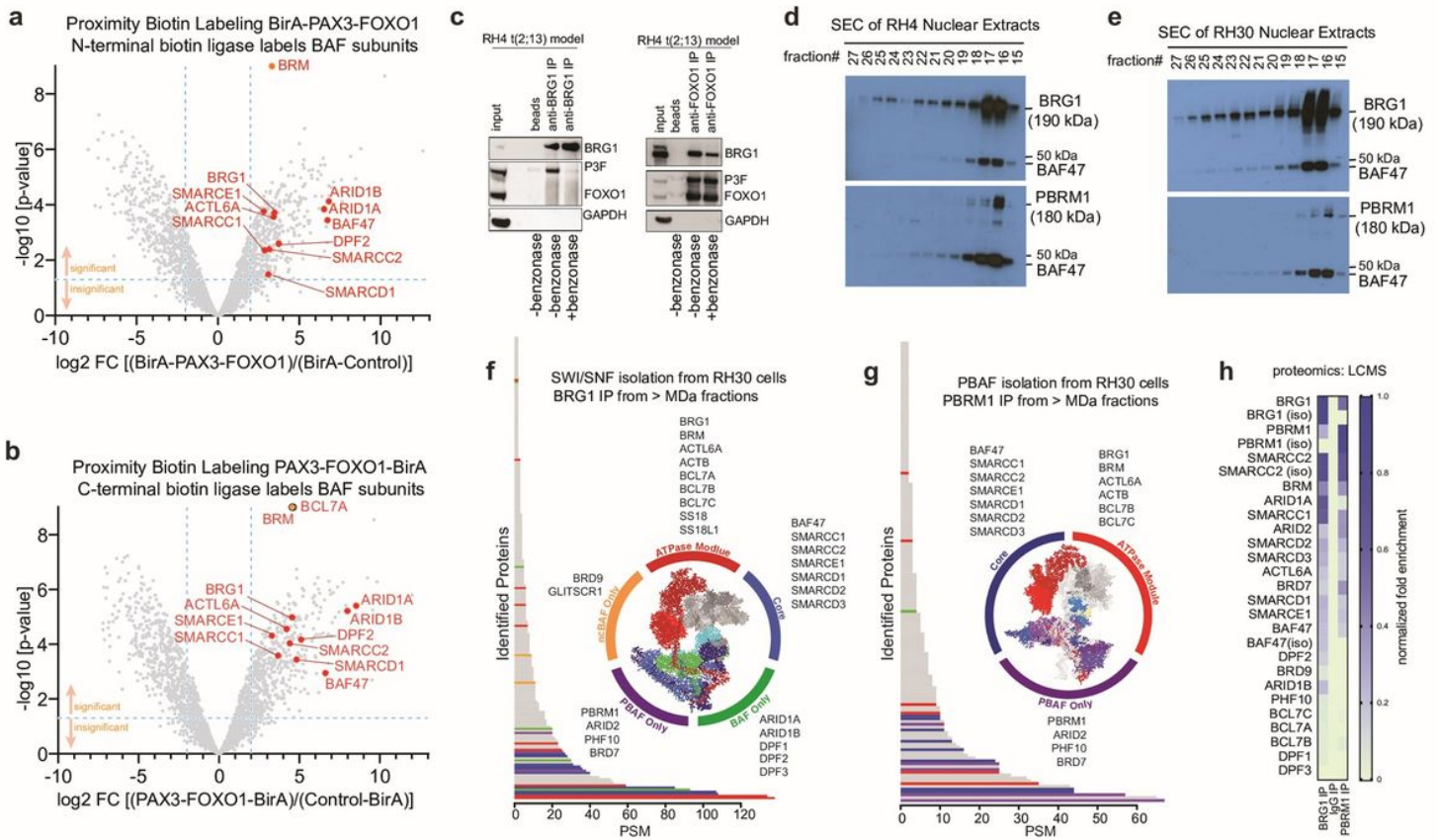


Figure 2

PAX3-FOXO1 shares spatial proximity with BAF subunits but is not incorporated into stable complexes. (a & b) Volcano-plots of PAX3-FOXO1 BioID experiments conducted in HEK293T cells. Mass spectrometry was performed on Strep-IP samples after either N- or C-terminal BirA tagged PAX3-FOXO1 and BirA only overexpression. Data points represent comparative protein signal intensities quantified by MaxQuant

software of 4 biological replicates. Significant enriched proteins ($p < 0.05$) with a $\log_2FC > 2.5$ in Pax3-FOXO1/BirA compared to BirA only Strep-IP samples are found in the upper right quadrants. mSWI/SNF complex members within this section are labelled. (c) Western blot detection of indicated endogenous proteins in anti-BRG1 or anti-FOXO1 immunoprecipitates from RH4 cells. Beads served as negative control. Lysates were digested or not with 250 U/ml Benzonase. (d & e) Size-exclusion chromatography (SEC) performed on RH4 and RH30 FP-RMS cell lines, followed by Western blotting the fractions for BRG1, BAF47 or PBRM1. Internal standards indicate fractions 15/16 are > 1 megadalton. (f&g) Proteins of BRG1 and PBRM1 SEC-IP LCMS experiments from RH30 cells are ranked in order of abundance (y-axis) and plotted as a function of peptide spectrum matches (PSM; x-axis). Inset shows RMS-specific BRG1 and PBRM1 associated proteins from summary proteomics experiments, color coded for subcomplex specificity (29 [f], 30[g]). (h) Heatmap (scale, inset) showing ranked mSWI/SNF subunits in FP-RMS, from BRG1, PBRM1, and IgG SEC IP LCMS experiments (iso = distinct isoform).

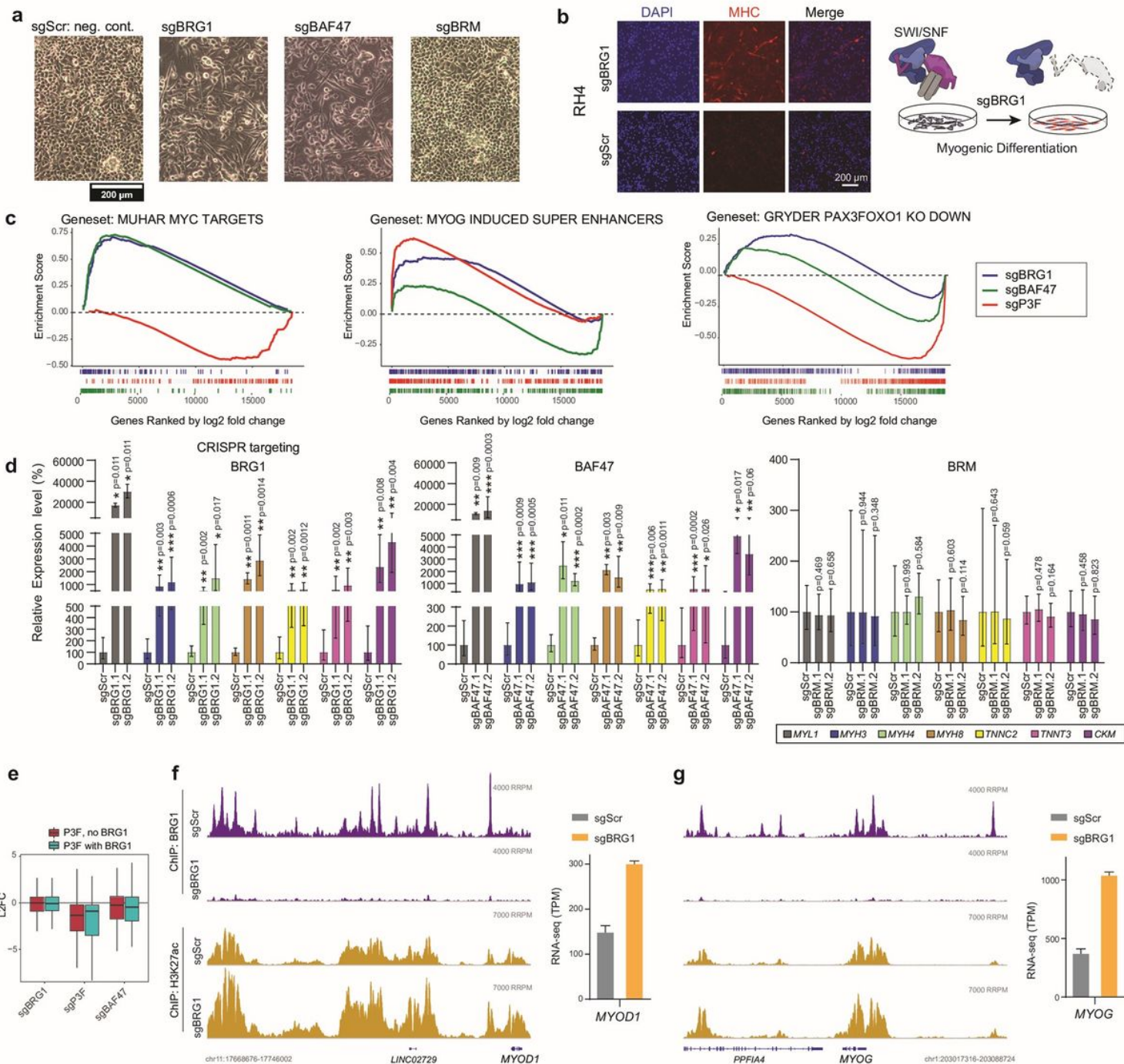


Figure 3

BAF complexes mediate myogenic differentiation blockade in FP-RMS. (a) Phase contrast images for morphology in Cas9 expressing RH4 cells 7 days after transduction with indicated sgRNAs with inset scalebar. (b) Immunofluorescence staining for DAPI (left panel), Myosin heavy chain (middle panel), or merged images (right panel) for either BRG1 knockout cells (top) or control cells (bottom) 7 days after transduction. (c) GSEA analysis of RNA-seq experiments of Cas9 expressing RH4 cells transfected with either guide RNAs against BRG1, BAF47 or PAX3-FOXO1 compared to negative control 7 days after transduction. (d) Relative mRNA expression levels of muscle differentiation marker genes 7 days after transduction of Cas9 expressing RH4 cells with indicated sgRNAs measured by quantitative real-time

PCR. Ct values relative to negative control sgRNA transduced cells were normalized to GAPDH expression. Mean and upper and lower level values are indicated for at least 3 independent biological replicates. Statistical significance (based on dCt values, rounded to last decimal) is given compared to negative control by paired t-tests. (* $p \leq 0.05$, ** $p \leq 0.01$, *** $p \leq 0.001$). (e) Differential expression levels of genes bound by PAX3-FOXO1 according to presence or absence of mSWI/SNF complex co-occupancy. (f&g) Genome browser tracks showing MYOD1 and MYOG loci for Spike-in normalized ChIP-seq experiments performed in RH4 cells after BRG1 knockout (sgBRG1) compared to negative control (sgScr) 7 days after transduction. Inserts show relative expression levels of MYOD1 and MYOG for the same time point as evaluated in RNA-seq experiments (TPM).

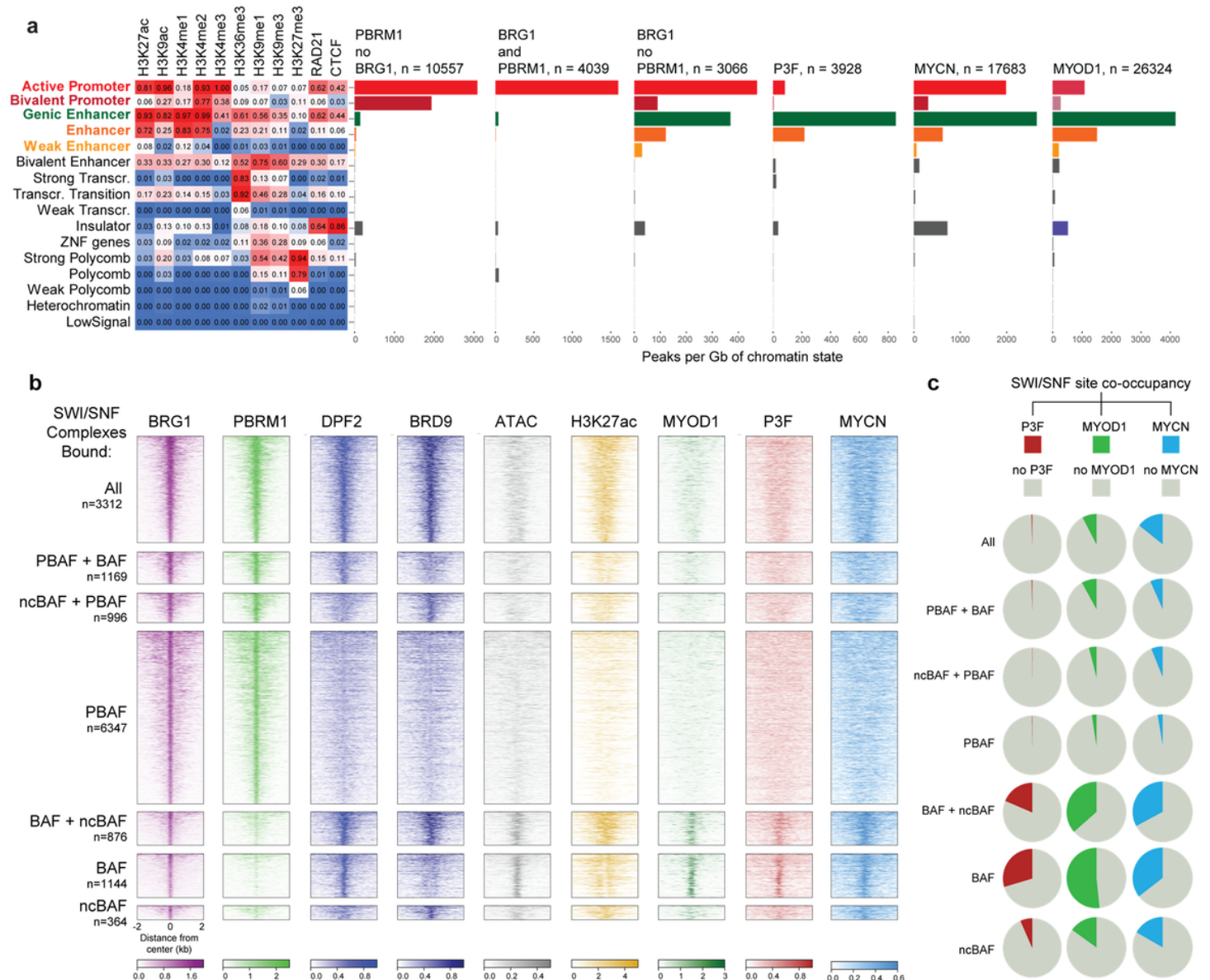


Figure 4

RMS-BAF complexes bind core regulatory circuitry. (a) Chromatin states in FP-RMS cells using ChIP-seq data for histone marks plus CTCF and RAD21 using hidden Markov modeling algorithm chromHMM are ranked for association with binding of PBRM1 alone, PBRM1 together with BRG1 or BRG1 alone, as well

as PAX3-FOXO1, MYCN and MYOD1 genomic binding. (b) Heat maps displaying peak distribution of BRG1, PBRM1, DPF2 and BRD9. Subtype complexes are defined as follows; BAF; BRG1 and DPF2, PBAF; BRG1 and PBRM1, ncBAF; BRG1 and BRD9. Additionally, H3K27ac deposition, as well as MYOD1, P3F and MYCN binding are given for BAF complex subtype specific sites. Number of detected peaks are indicated on the left. (c) Pie-charts illustrating degree of co-occupancy of BAF complex subtype bound loci with PAX3-FOXO1, MYOD1 and MYCN.

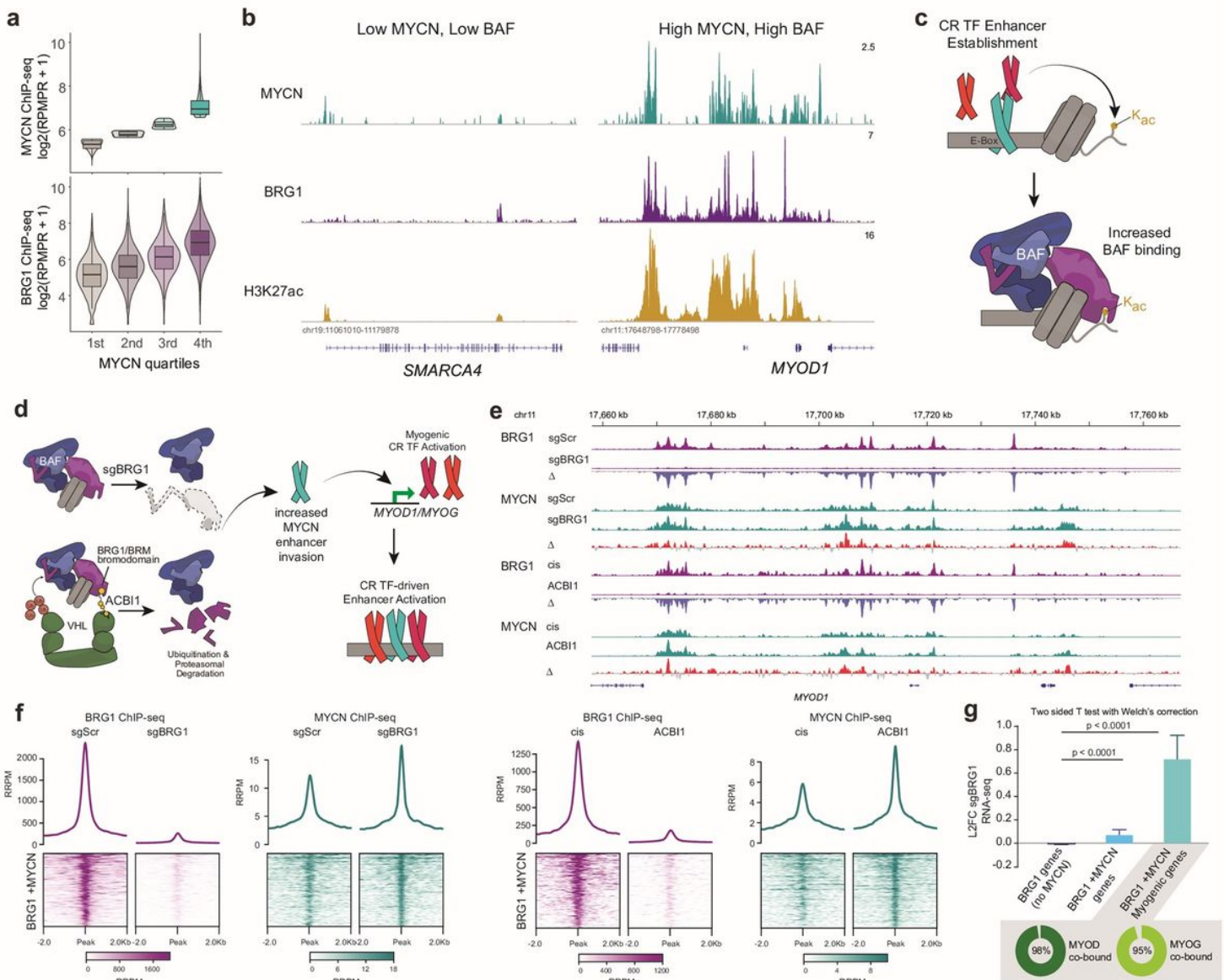


Figure 5

BRG1 responds to and refines the FP-RMS core transcriptional circuitry. (a) ChIP-seq peak distribution of BRG1 in comparison to MYCN peak intensities. Subdivision of MYCN peaks into quartiles reveals positive correlation between MYCN and BRG1 binding. (b) ChIP-seq browser tracks of BRG1, MYCN and H3K27ac for SMARCA4 and MYOD1 associated loci. (c) Proposed model for CRTF enhancer/promoter establishment, inducing H3K27 acetylation, leading to recruitment of BAF complexes. (d) A proposed model for genetic ablation of BRG1 vs. chemical degradation of BRG1/BRM, activating myogenesis. (e)

Browser snapshot of the MYOD1 locus showing binding patterns of BRG1 and MYCN after removal of BRG1 (genetically or chemically). (f) Genetic or chemical depletion of BRG1 followed by CHIP-Rx (reference exogenous reads per million mapped reads, RRPm) resulting in BRG1 removal yet an increase in MYCN binding at these same co-occupied sites (n = 1,904). (g) RNA-seq of genes associated with BRG1 only peaks, BRG1 with MYCN sites, or a subset of BRG1 with MYCN at myogenic genes. Data is shown as the median and error bars show the 95% confidence interval of the log2 fold change in expression after sgBRG1.

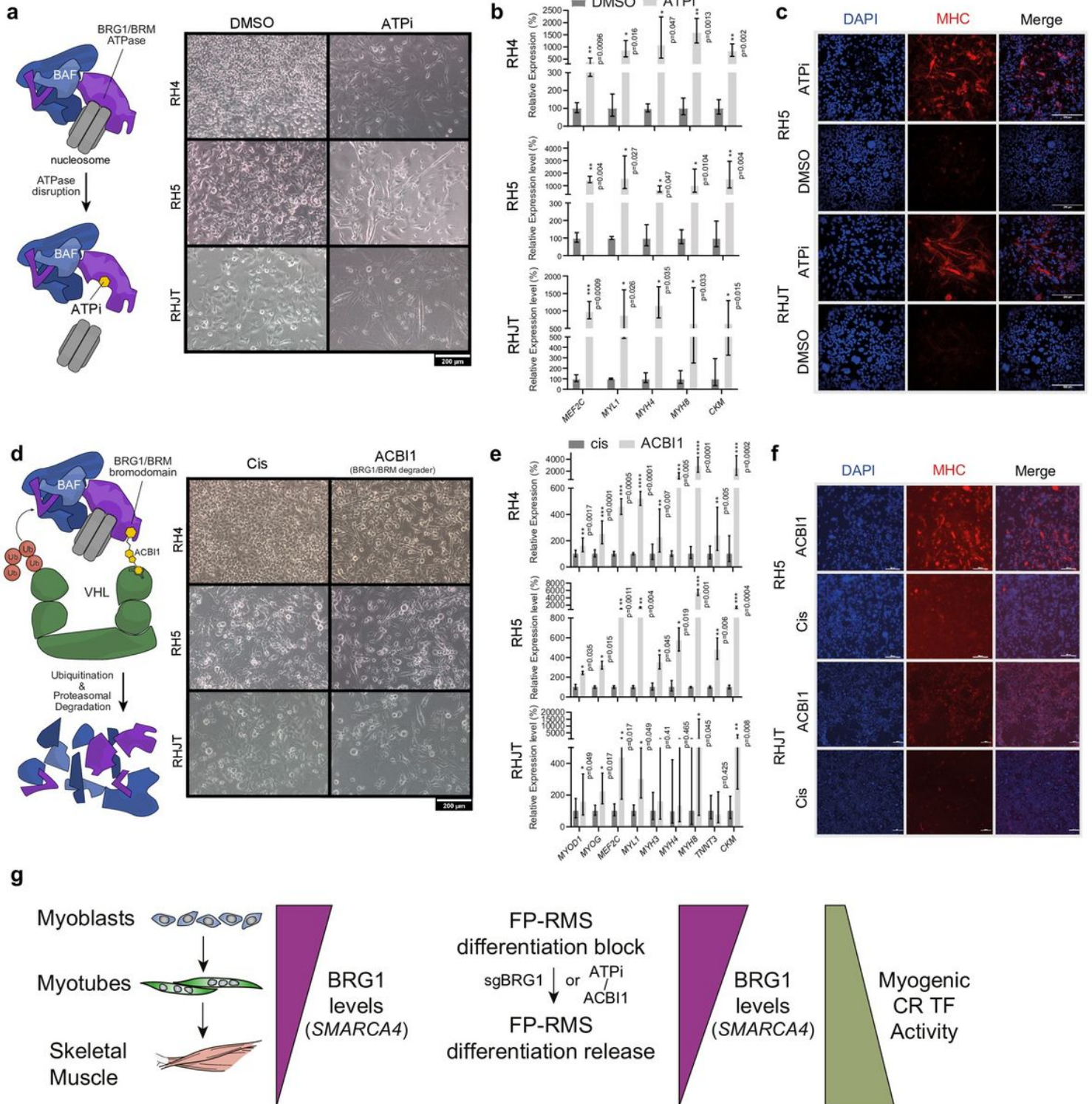


Figure 6

BRG1/BRM inhibiting compounds induce myogenic differentiation in FP-RMS cell lines. (a-c) Effects of ATPase inhibitor treatment (3 μ M) and (d-e) Effects of ACBI1 PROTAC compound treatment (250nM), with Cis conformation compound used as negative control on different FP-RMS cells after 72 hours. (a, d) Phase contrast images with inset scale bars in indicated cell lines (b,e) Relative mRNA expression levels of muscle differentiation marker genes measured by quantitative real-time PCR. Ct values relative to DMSO treated cells were normalized to GAPDH expression. Mean and upper and lower level values are indicated for at least 3 independent biological replicates. Statistical significance (based on dCt values, rounded to last decimal) are given compared to negative control by paired t-tests. (* $p \leq 0.05$, ** $p \leq 0.01$, *** $p \leq 0.001$). (c, f) Immunofluorescence staining for DAPI (left panel), Myosin heavy chain (middle panel), or merged images (right panel) for either control (bottom) or compound treated cells (top). (g) Model of BRG1 function in normal myogenesis compared to its contribution to differentiation blockade in FP-RMS.

Supplementary Files

This is a list of supplementary files associated with this preprint. Click to download.

- [TableS1.xlsx](#)
- [TableS2.xlsx](#)
- [TableS3.xlsx](#)
- [TableS4.xlsx](#)
- [TableS5.xlsx](#)
- [SupplementaryFigures.pdf](#)
- [SourceData.xlsx](#)